

X-ray sources within the central parsec. These sources are spectrally consistent with quiescent XRBs and distinct from the magnetic CVs that make up most of the X-ray sources outside of the central parsec. Additionally, their luminosity function is consistent with that of dynamically confirmed BH XRBs in the field, while NSs are on average brighter in quiescence (Armas Padilla et al. 2014; Hailey et al. 2018). Other confirmed NS XRBs with comparable X-ray luminosities in the Galactic Center region and globular clusters show bright outbursts with a characteristic cadence of 5–10 years (Degenaar & Wijnands 2010; Bahramian et al. 2014); the exceptions are almost all thermal sources, and therefore not directly comparable to the GC population. Thus, if the quiescent population were NS-XRBs, there would be many more outbursts than are observed. It is possible that there is an undiscovered class of NS-XRBs that mimic the properties of BH-XRBs. Nonetheless, the most likely identification for this new population is quiescent BH XRBs, though an admixture of up to six millisecond pulsars cannot be ruled out. Reasonable extrapolation of the point source luminosity function below the instrumental detection threshold implies hundreds of BH-XRBs inside the central parsec.

The number of NS XRBs per stellar mass in the GC is three orders of magnitude greater than in the field, and comparable to the number in Globular clusters (see Table 1). The number of BH XRBs per stellar mass in the GC is also three orders of magnitude greater than in the field, and an order of magnitude greater than in any existing globular, suggesting the GC BH XRBs are not brought in via globular cluster in-fall. Also, any BH XRBs brought in by globulars are unlikely to survive to the present day, as the lifetime of BH XRBs is at most a few $\times 10^9$ years (see Fig. 10).

This indicates that the unusual environment of the GC dynamically - and efficiently - assembles BH-XRBs, in a manner analogous to the dynamical overproduction of NS-XRBs in globular clusters (Katz 1975; Benacquista & Downing 2013). Although a high concentration of compact objects in the GC is itself unsurprising (Alexander & Hopman 2009), an overabundance of mass-transferring *binaries* is more challenging to understand. In other dense stellar systems like globular clusters, exchange interactions that swap compact objects into binaries can explain the overabundance of NS-XRBs and their MSP progeny (e.g. Ivanova et al. 2008). However, this channel is strongly suppressed in NSCs because nearly all primordial stellar binaries would be evaporated by three-body encounters, and those that survive would be so hard as to present a minimal cross-section for exchange interactions (see Leigh et al. 2018 and appendix C).¹

This paper instead focuses on an alternative channel of XRB formation: the tidal capture of main sequence stars by compact objects (Press & Teukolsky 1977; Lee & Ostriker 1986). Stars that pass sufficiently close to a compact object—approximately, within its tidal radius r_t —are completely torn apart by tidal forces (e.g. Rees 1988). However, for pericenter radii somewhat larger than r_t , tidal forces are not necessarily destructive; instead, they transfer orbital en-

ergy into internal oscillations of the star, binding it to the compact object. Following a complex and potentially violent process of circularization, the newly-created binary settles into a tight orbit. The necessarily small orbital separation of the tidal capture binary guarantees that subsequent gravitational wave emission will drive the star into Roche Lobe overflow in less than a Hubble time, forming a mass-transferring X-ray source. The high density of compact objects and stars in the GC inevitably lead to a significant rate of tidal captures, representing a promising explanation for the observed overabundance of BH- and NS-XRBs.

This paper is organized as follows. In § 2 we describe our model for the dynamical evolution of stars and compact remnants in the GC. In § 3 we use the time-dependent density profiles of the stars and compact objects from our NSC models to calculate the rates of collisions and tidal capture of stars by compact objects, and make predictions for the present-day BH and NS-XRB population. In § 4 we compare our predictions to observations of the XRB populations in the GC measured by Hailey et al. (2018). In § 5 we describe several auxiliary predictions of our model for the rates of stellar interactions and exotic transients. In § 6 we briefly summarize our results and conclude.

2 GALACTIC NSC MODEL

The number of BH-XRBs that form in the GC clearly depends on the number of stellar-mass BHs that reside there. Previous works have predicted that $\gtrsim 10^3 - 10^4$ BHs accumulate within the central parsec over timescales of several Gyr due to radial mass segregation from the stellar population on larger scales (e.g. Morris 1993; Miralda-Escudé & Gould 2000; Freitag et al. 2006; Hopman & Alexander 2006b; O’Leary et al. 2009; Dale et al. 2009; Merritt 2010). Most previous models assume that the BHs are distributed at birth in the same way as the lower mass stars, and neglect ongoing star formation (though see Aharon & Perets 2015; Baumgardt et al. 2018).

In fact, much of our NSC’s total stellar population was likely deposited by the infall of globular clusters early in its history (Tremaine et al. 1975; Antonini et al. 2012; Gnedin et al. 2014; Arca-Sedda & Capuzzo-Dolcetta 2014; Abbate et al. 2018; Arca-Sedda et al. 2017). Historically, globular clusters (at least of the kind which survive to the present day) were predicted to lose all but a few of their BHs due to strong kicks in multi-body interactions during a core collapse or Spitzer instability phase (e.g. Spitzer 1987; Kulkarni et al. 1993; Banerjee et al. 2010). Such lossiness would limit the ability of globular infall to seed the GC with BHs, although modern studies have challenged this conventional wisdom by showing that $\sim 10^2 - 10^3$ BHs could be retained in globulars due to three-body processes reversing core collapse (Mackey et al. 2008; Morscher et al. 2013, 2015; Askar et al. 2018; Kremer et al. 2018b).² While a few candidate globular cluster BH-XRBs have been identified in the MW (Strader et al. 2012b; Bahramian et al. 2017), and other

¹ Note that the maximum semi-major axis above which binaries are evaporated scales as velocity dispersion σ^{-2} , whereas the maximum pericenter for tidal capture scales $\sigma^{-0.2}$; see appendix C for more details.

² Physically, this is because the thermodynamics of the subcluster is regulated by the longer relaxation time of the bulk cluster (Breen & Heggie 2012, 2013).

Table 1. Estimated abundances of NS-XRB/BH-XRB/MSP per unit stellar mass in different environments. Q=Quiescent LMXBs ($L_x \lesssim 10^{33}$ erg s $^{-1}$); T=Transient LMXBs; B=Persistently bright or transient LMXBs (only persistently bright sources are NSs). No outbursts have been seen from globular BH XRB candidates, while only one quiescent BH XRB candidate has been identified in the field (Tetarenko et al. 2016). The abundances in the “transient” BH-XRB column estimate the total population of BH-XRBs prone to periodic outburst, computed by assuming that the observed BH-XRB transients represent a larger population with a characteristic recurrence time of 100 years.

| Environment | $N_{\text{NS-XRB}} \text{ (B)}$ [M_{\odot}^{-1}] | $N_{\text{NS-XRB}} \text{ (Q)}$ [M_{\odot}^{-1}] | $N_{\text{BH-XRB}} \text{ (T)}$ [M_{\odot}^{-1}] | $N_{\text{BH-XRB}} \text{ (Q)}$ [M_{\odot}^{-1}] | N_{MSP} | References |
|----------------------------------|---|---|---|---|-------------------------------|------------|
| Field | 2×10^{-9} | – | 2×10^{-8} | – | 5×10^{-9} | 1-3 |
| Globular clusters (all) | 3×10^{-7} | 6×10^{-7} | – | 10^{-7} | 7×10^{-6} | 5-7 |
| 47 Tuc | – | 7×10^{-6} | – | 10^{-6} | 3×10^{-5} | 8-11 |
| Terzan 5 | 1.5×10^{-6} | 6×10^{-6} | – | – | 2×10^{-5} | 12-13 |
| Galactic Center (central parsec) | $1 - 3 \times 10^{-6}$ | – | 2×10^{-5} | 10^{-5} | $\lesssim 1.3 \times 10^{-4}$ | 14-18 |

References (1) Corral-Santana et al. (2016) (2) Tetarenko et al. (2016) (3) Galactic MSPs (4) Benacquista & Downing (2013) (5) Strader et al. (2012a) (6) Strader et al. (2012b) (7) Globular MSPs (8) Miller-Jones et al. (2015) (9) Bahramian et al. (2017) (10) Heinke et al. (2005b) (11) Heinke et al. (2005a) (12) Heinke et al. (2006) (13) Bahramian et al. (2014) (14) Degenaar et al. (2015) (15) Munro et al. (2005) (16) Hailey & Mori (2017) (17) Hailey et al. (2018) (18) Perez et al. (2015)

BH-XRBs have been seen in extragalactic globulars (Maccarone et al. 2007), the total inventory of globular BHs is challenging to infer from observations because the number of BH-XRBs is likely a weak function of the number of retained BHs (Kremer et al. 2018a). Overall, if globulars retain an order unity fraction of their BHs they can deliver $\sim 2 \times 10^4$ BHs to the Galactic Center (Arca-Sedda et al. 2017).

A potentially larger population of BHs is formed in the GC by *in situ* star formation. A disk of young stars of age ≈ 4 Myr is observed to extend between $\sim 0.03 - 0.3$ pc of SgrA* (Krabbe et al. 1995; Paumard et al. 2006; Lu et al. 2013), containing a total of ~ 100 WR/O stars with a top-heavy initial mass function (IMF; e.g. Bartko et al. 2010; Lu et al. 2013). If the average formation rate of massive stars is comparable to the rate in the last few million years, a total of $\sim 10^5$ compact objects would be injected into the Galactic Center over 10 Gyr. However, there is no evidence for multiple bursts of star formation over the last few $\times 10^7$ years (Habibi et al. 2017)³, and feedback from stellar winds and Supernovae would suppress star formation on this time-scale. This suggests star-bursts occur with a cadence of at least 4×10^7 years. In principle, the cadence may be much longer, but this would mean we are observing the GC at a very atypical time. In this paper, we focus on models with bursts of star formation every $4 \times 10^6 - 4 \times 10^7$ years.

This section describes our prescription for how the 1D radial density profiles of stars and compact remnants in the GC evolve in time. Our goal is to create a small set of simple but physically-motivated models for building up the NSC, that are consistent with both the present-day stellar density profile and the observed rate of compact object formation. Motivated by the above discussion, our model consists of two stellar populations: (1) stars injected in the distant past, near the formation time of the NSC; and (2) a continuously forming *in-situ* population with a top heavy IMF concentrated within the central parsec, as is motivated by the observed disks of young stars (Lu et al. 2013). All of our models assume spherical symmetry and isotropic velocities.

In §2.1 we motivate the parameters of our models using

³ The existing stellar population would not probe the star formation history on longer time-scales if the IMF is truncated below $\sim 10 M_{\odot}$

the observed stellar populations and constraints on the star formation history in the GC. In § 2.2 we describe our numerical procedure for evolving the density profiles of stars and compact objects through two-body relaxation. To build up physical intuition, we first calculate how the compact objects evolve in isolation in § 2.3, before adding the effects of the stellar background in § 2.4. In § 2.5 we discuss several additional hypothetical scenarios for building the NSC, in order to assess the uncertainty in our work and to make contact with previous papers in the literature (which generally neglect centrally-concentrated compact object formation).

2.1 Stellar and Compact Object Populations

Eighty percent of the stars in the GC are older than 5 Gyr (Pfuhl et al. 2011), consistent with the bulk of the NSC’s growth being due to the infall of globular clusters via dynamical friction over a period of ~ 1 Gyr in the early history of the Galaxy (Gnedin et al. 2014). The observed diffuse stellar light⁴ is well fit by the parameterization (Schödel et al. 2018; their Tables 2 and 3),

$$\rho_{\star}(r) = 2^{(\beta-\gamma)/\alpha} \rho_0 \left(\frac{r}{r_0}\right)^{-\gamma} \left(1 + \left(\frac{r}{r_0}\right)^{\alpha}\right)^{(\gamma-\beta)/\alpha}, \quad (1)$$

with best-fit parameters of $\gamma = 1.16 \pm 0.02$, $\beta = 3.2 \pm 0.3$, $r_0 = 3.2 \pm 0.2$ pc for fixed $\alpha = 10$. The density normalization at 1 pc is $0.8 - 1.7 \times 10^5$ pc $^{-3}$.⁵

Compact objects are also deposited at early times if they arrive with the globular clusters. Ivanova et al. (2008) estimate that a typical globular cluster retains 1 NS per

⁴ This profile differs from the observed giant density profile, which has a core inside of ~ 0.5 pc (the so-called “missing giants” problem; e.g. Buchholz et al. 2009; Do et al. 2009). The diffuse light tracks emission from early G and late F main sequence and sub-giant stars, and is likely a better probe of the underlying stellar density. One solution to the missing giants problem is mass-stripping by collisions between the giants with other stars and compact objects (Dale et al. 2009) or with a clumpy gas disc (Amaro-Seoane & Chen 2014; Kieffer & Bogdanović 2016).

⁵ We use the values from the first version of Schödel et al. (2018). The best fit parameters are slightly different in the published version, but consistent within uncertainties.

$10^3 M_\odot$ of other stars. Although globulars may also bring in a sizeable BH population, this is less certain because, as discussed above, BHs may be ejected from globulars by binary-single interactions (e.g. Kulkarni et al. 1993; Banerjee et al. 2010; see, however, Morscher et al. 2015). Given this uncertainty, and because the current BH population is anyways likely to be dominated by *in situ* star formation (see below), we neglect BHs deposited with the old stellar population.

Our fiducial models include a population of compact objects formed *in situ*, motivated by the sub-parsec disk of young stars observed in the GC. The K-band luminosity function of the young stars is consistent with a single starburst that occurred 2.5–5.8 Myr ago (Lu et al. 2013; Habibi et al. 2017). The burst produced a total of ~ 250 stars of mass $\gtrsim 8 M_\odot$ with an IMF of the form $dN/dm \propto m^{-\beta}$ with $\beta \approx 1.7$. If stars with masses in the range $m \approx 8 - 25 M_\odot$ form NSs, while those with $m \gtrsim 25 M_\odot$ form BHs, then a total of $N_{\text{ns}} \sim 160$ NSs and $N_{\text{bh}} \sim 90$ BHs were, or will be, formed from the disk stars. If the time since the last star formation episode of ≈ 4 Myr is comparable to the typical interval between starbursts, then the implied average formation rates of NSs and BHs in the central parsec are $\dot{N}_{\text{ns}} \sim 4 \times 10^{-5} \text{ yr}^{-1}$ and $\dot{N}_{\text{bh}} \sim 2 \times 10^{-5} \text{ yr}^{-1}$, respectively.

The above estimates assume that the current epoch is a representative snapshot of the central parsec’s average star formation history. In possible tension with this, Pfuhl et al. (2011) find that the star formation rate $\sim 1 - 5$ Gyr ago was $\sim 1 - 2$ orders magnitude smaller than the present-day rate (their Figure 14), in which case the average star formation rate is $\lesssim 10\%$ of its recent value. However these observations probe only low mass stars ($\lesssim 2 M_\odot$), and thus do not constrain the rate of NS/BH formation within the star-forming disks if the top-heavy disk IMF is truncated below a few solar masses. Other nearby galactic nuclei such as M31 possess disks of A stars, but no O and B stars (Leigh et al. 2016); in these NSCs at least, the last major episode of star formation occurred $\gtrsim 100$ Myr ago.

Motivated by the above, we construct our fiducial models for the GC using the following three populations:

- “Primordial” stars, which are assumed to form impulsively at $t = 0$ (10 Gyr ago) with an initial density profile following eq. (1). We model all the stars as being of a single mass $0.3 M_\odot$, which represents the root-mean-square mass of main sequence and sub-stellar objects in an evolved Kroupa IMF. For simplicity, the parameters of the stellar profile (α, β, γ) are fixed to the best-fit values from Schödel et al. (2018), except for the scale radius r_o and normalization ρ_o . The cluster expands radially over time, so we chose smaller initial values of $r_o = 0.5, 1.5$ pc in order to match the *present-day* stellar density at 1 pc (though we note that the functional form of the density profile is not exactly preserved in the evolution). A normalization of $\rho_*(1 \text{ pc}) = 1.1 \times 10^5 M_\odot \text{ pc}^{-3}$ is chosen to fix the total stellar mass to $5.7 \times 10^7 M_\odot$.⁶
- “Primordial” NSs of mass $1.5 M_\odot$, which are deposited

⁶ The true total mass, $2.5 \pm 0.4 \times 10^7 M_\odot$, is somewhat lower. The difference comes from the fact that we assume the stellar density profile extends to infinity (with an $r^{-3.2}$ profile), but in reality the stellar density steepens at ~ 10 pc.

impulsively at $t = 0$ with the same density profile as the stars. The total number of NSs is normalized to a fraction 10^{-3} of the number of stars, motivated by their expected abundance in globular clusters (Ivanova et al. 2008).

- Compact objects from *in situ* star formation (NSs and BHs of masses 1.5 and $10 M_\odot$, respectively) that are continuously injected near the present-day disk of young stars. The source term is narrowly peaked at the potential energy at 0.3 pc (the outer edge of the disk). In physical space, star formation is concentrated inside of this radius with an $r^{-0.5}$ density profile. We found our results do not change if the star formation is instead concentrated inside of 0.03 pc (the inner edge of the star forming disks). In our “**Fiducial**” model, we adopt conservative formation rates of $\dot{N}_{\text{ns}} = 4 \times 10^{-6} \text{ yr}^{-1}$ and $\dot{N}_{\text{bh}} = 2 \times 10^{-6} \text{ yr}^{-1}$, respectively. We also consider a model (“**Fiducial** $\times 10$ ”) in which \dot{N}_{ns} and \dot{N}_{bh} are ten times larger, corresponding to the present day formation rate of massive stars.

The parameters of our fiducial models are summarized in Table 2. Several hypothetical (non-fiducial) models are introduced in §2.5 in order to assess the robustness of our conclusions.

2.2 Numerical Method: Fokker-Planck

The radial distribution of stars and compact objects evolves over time due to two-body relaxation. We follow this evolution using the PHASEFLOW code (Vasiliev 2017), which solves the time-dependent, isotropic Fokker-Planck equation for the energy-space distribution function $f(\epsilon, t)$. This equation can be written in flux-conserving form as

$$\frac{\partial f(\epsilon, t)}{\partial t} = - \frac{\partial}{\partial \epsilon} \left[\underbrace{D_{\epsilon\epsilon} \frac{\partial f(\epsilon, t)}{\partial \epsilon} + D_\epsilon f(\epsilon, t)}_{F(\epsilon)} \right] - \frac{f(\epsilon, t)}{\tau_{\text{LC}}(\epsilon, t)} + S(\epsilon, t), \quad (2)$$

where ϵ is the binding energy, D_ϵ and $D_{\epsilon\epsilon}$ are the first and second order energy diffusion coefficients, $F(\epsilon)$ is the mass flux, and the last two terms account for the draining of stars into the loss cone of the SMBH (see eq. 13 in Vasiliev 2017), and injection of stars due to star formation. The diffusion coefficients can be expressed as integrals over the distribution function, which for a single species mass m are given by

$$D_{\epsilon\epsilon} = 16\pi^2 G^2 m \ln \Lambda \left[h(\epsilon) \int_0^\epsilon f(\epsilon') d\epsilon' + \int_\epsilon^{\epsilon_{\text{max}}} f(\epsilon') h(\epsilon') d\epsilon' \right] \quad (3)$$

$$D_\epsilon = -16\pi^2 G^2 m \ln \Lambda \int_\epsilon^{\epsilon_{\text{max}}} f(\epsilon') g(\epsilon') d\epsilon', \quad (4)$$

where $h(\epsilon)$ is the phase volume and $g(\epsilon) = dh(\epsilon)/d\epsilon$ is the density of states (see e.g. Merritt 2013). For a Keplerian potential, $h \propto \epsilon^{-3/2}$ and $g \propto \epsilon^{-5/2}$.

The one-dimensional Fokker-Planck approach is computationally efficient and reproduces the results from two-dimensional Fokker-Planck (Cohn 1985; Merritt 2015) as well as Monte-Carlo and N-body calculations (Vasiliev 2017) reasonably well. A key assumption of this equation is spherical symmetry, which is in tension with the physical motivation for our source term $S(\epsilon, t)$: disk-mode star formation.

However, it is reasonable to assume that compact remnants will become isotropic over time. First of all, there is likely no preferred plane for disk mode star formation in the GC. The current disk of young stars is not aligned with either the Galactic disk or the circumnuclear ring of molecular gas (McCourt & Madigan 2016). Thus, the injected remnants from many different episodes of *in situ* star formation would naturally form with a quasi-isotropic angular distribution. Recent work has found that vector resonant relaxation can lead to a disk configuration for BHs and heavy stars even if they are drawn from sixteen randomly oriented disks (Szölgvény & Kocsis 2018). However, as the number of star formation episodes increases, the disk would thicken and would approach an isotropic distribution (Bence Kocsis, personal communication). In principle, resonant relaxation (Rauch & Tremaine 1996; Hopman & Alexander 2006a) may flatten the radial stellar density profile by causing stars to diffuse more rapidly into the loss cone. In practice, this effect only becomes important on small radial scales $\lesssim 0.1$ pc (Bar-Or & Alexander 2016), interior to where most tidal captures occur.

Finally, strong gravitational scatterings by BHs can lead to significant evaporation of low mass stars and remnants from the cusp. This effect is not included in our models, but a post-hoc calculation shows it changes the stellar density profile by $\lesssim 40\%$ (see § 2.6).

2.3 Evolution with Compact Remnants Only

Compact objects which are injected near the present disk of massive stars at ~ 0.3 pc will diffuse outwards via two-body scattering. To study this process, we solve eq. (2) with a constant source function of injected BHs, $\dot{N}_{\text{bh}} = 2 \times 10^{-5} \text{ yr}^{-1}$, corresponding to our “Fiducial $\times 10$ ” model. To whet our intuition in a controlled setting, we initially neglect contributions to the gravitational potential or diffusion coefficients from the background of NSs and stars.

Figure 1 (top panel) shows the resulting BH number density profile $n(r)$ after 10 Gyr of evolution, over which a quasi-steady state is achieved on small radial scales. For comparison, a dashed line shows how little the solution changes if one neglects the gravitational potential of the stellar mass BHs and the loss cone sink (the final term in eq. 2). The steady-state BH profile is well described by a broken power law, with $n \propto r^{-7/4}$ at small radii $r \ll r_i$ and $n \propto r^{-5/2}$ at $r \gg r_i$. These power-law slopes and the normalization of the BH profile can be understood through basic analytic arguments.

Compact objects injected at r_i diffuse outwards on the two-body relaxation timescale, which for a single mass population m_c is approximately given by⁷,

$$\tau_{\text{rx}} \approx \frac{0.34}{\log \Lambda} \frac{\sigma^3(r)}{G^2 n(r) m_c^2}, \quad (5)$$

where $\sigma(r)$ is the one dimensional velocity dispersion, $n(r)$ is the number density, and $\log \Lambda \approx 15$ is the Coulomb logarithm.

⁷ For a Keplerian potential, the pre-factor of eq. (5) varies from 0.2–0.4, depending on the density profile power-law slope $\gamma = 0.5 - 3$, where $n \propto r^{-\gamma}$.

In a steady state, the formation rate of compact objects per unit volume equals the rate of outwards diffusion, i.e.

$$\frac{\dot{N}}{r_i^3} \sim \frac{n_i}{\tau_{\text{rx}}(r_i)}. \quad (6)$$

This implies a steady-state density at the injection radius of

$$n(r_i) \propto r_i^{-9/4} \dot{N}^{1/2} M^{3/4} m_c^{-1}, \quad (7)$$

where in taking $\sigma \propto (GM/r)^{1/2}$ we have assumed that the SMBH of mass M dominates the gravitational potential. Normalizing equation (7) using results from our numerical solutions, we find

$$n_i = 1.6 \times 10^4 \left(\frac{r_i}{0.3 \text{ pc}} \right)^{-9/4} \left(\frac{\dot{N}}{2 \times 10^{-5} \text{ yr}^{-1}} \right)^{1/2} \left(\frac{M}{4 \times 10^6 M_\odot} \right)^{3/4} \left(\frac{m_c}{10 M_\odot} \right)^{-1} \text{ pc}^{-3}, \quad (8)$$

What sets the power-law slopes of the BH density profile? For a distribution function $f \propto \epsilon^p$ which extends to a maximum energy ϵ_{max} , the flux of mass through energy space (see eq. 2) is

$$F(\epsilon) \propto \epsilon^{2p-3/2} \left[a_o(p) + a_1(p) \left(\frac{\epsilon_{\text{max}}}{\epsilon} \right)^{p-3/2} + a_2(p) \left(\frac{\epsilon_{\text{max}}}{\epsilon} \right)^{p-1/2} \right] \\ a_o(p) = \frac{3(4p-1)}{(1+p)(2p-1)(2p-3)}, \quad (9)$$

where a_1 , a_2 , and a_3 are dimensionless functions of p .

In steady state, the flux through energy space is constant. For $p < 1/2$, one finds $F \approx a_o(p) \epsilon^{2p-3/2}$ in the limit that $\epsilon_{\text{max}} \rightarrow \infty$ and thus F will be zero for $p = 1/4$; this is the classical “Bahcall-Wolf” (BW) solution (Bahcall & Wolf 1976). If $p > 1/2$, the a_2 term in equation (9) dominates over the first two terms. A $p = 1$ profile corresponds to the steady-state solution with a constant, non-zero (outwards) flux. In this case ϵ_{max} must have a finite value, as otherwise the flux would diverge; in our case, this maximum energy corresponds to the location of the source function of injected BHs at r_i . These two steady state solutions (zero flux at small radii and constant outward flux at large radii) correspond to density profiles $n \propto r^{-7/4}$ and $\propto r^{-5/2}$, respectively. In this solution, energy is transferred from the injection radius to larger scales by stars on eccentric orbits. However, Fragione & Sari (2018) have argued that these stars cannot effectively transfer energy to the bulk of the stellar population and evolve in a decoupled way (an effect which the isotropic Fokker-Planck solver in PHASEFLOW cannot capture). In this case, energy relaxation at any radius would be dominated by the local stellar population, and by mass conservation the density has a slightly shallower $r^{-9/4}$ profile (see also Peebles 1972). Ultimately, the two-dimensional Fokker-Planck simulations are necessary to determine the correct outer density profile.

The enclosed mass $\propto nr^3 \propto r^{1/2}$ is dominated by the largest radius to which the BHs have time to diffuse over the system age t . The half-mass radius $r_{1/2}$, interior to which the above steady-state profile is established, can be estimated by equating the system age with the relaxation time; using

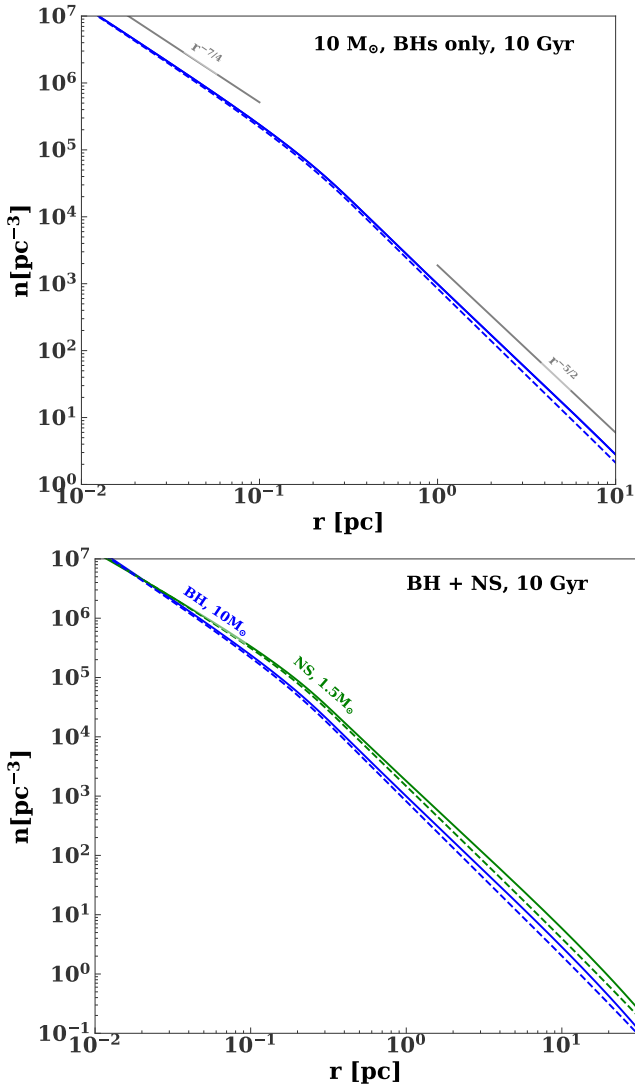


Figure 1. *Top panel:* Number density of BHs in the GC as a function of radius r after 10 Gyr of evolution, in the case of continuous BH injection (solid line). BHs are injected at a constant rate $\dot{N}_{\text{bh}} = 2 \times 10^{-5} \text{ yr}^{-1}$ at $r_{\text{in}} \approx 0.3 \text{ pc}$. *Bottom panel:* Density profiles of NSs and BHs after 10 Gyr of evolution for injection rates at r_i corresponding to our Fiducial $\times 10$ model ($\dot{N}_{\text{ns}} = 4 \times 10^{-5}$, $\dot{N}_{\text{bh}} = 2 \times 10^{-5} \text{ yr}^{-1}$). Dashed lines show how the results change if the gravitational potential of the compact objects, and the sink term due to SMBH loss cone, are neglected.

equation (5), this gives

$$r_{1/2} \approx 3.3 \text{ pc} \left(\frac{t}{3 \text{ Gyr}} \right)^2 \left(\frac{r_i}{0.3 \text{ pc}} \right)^{-1/2} \left(\frac{\dot{N}}{2 \times 10^{-5} \text{ yr}^{-1}} \right) \left(\frac{M}{4 \times 10^6 M_{\odot}} \right)^{-3/2} \left(\frac{m_c}{10 M_{\odot}} \right)^2. \quad (10)$$

BHs injected in the GC therefore have sufficient time to establish a steady-state profile within the central parsec by the present age ($t = 10 \text{ Gyr}$).

The bottom panel of Fig. 1 shows the present-day density profiles for a calculation otherwise identical to the BH-only case, but including the evolution of *both* the BHs and NSs, assuming each are injected at r_i at rates of $\dot{N}_{\text{bh}} =$

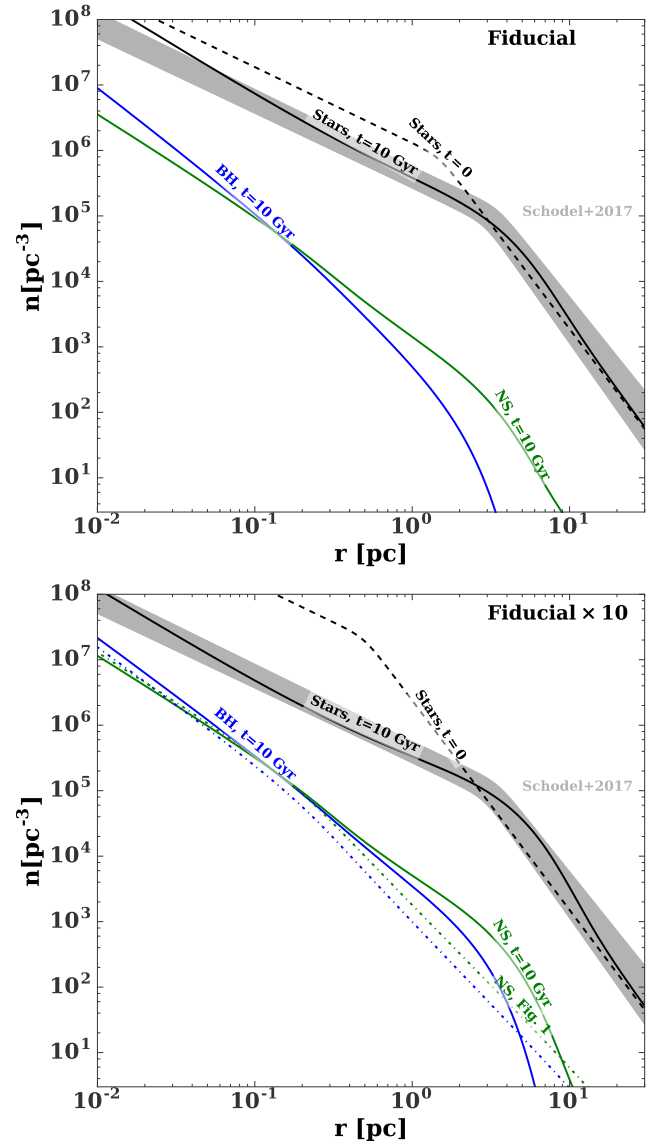


Figure 2. *Top panel:* Fiducial density profiles of stars and compact remnants at $t = 10 \text{ Gyr}$ (solid lines). Compact remnants are continuously injected near $\sim 0.3 \text{ pc}$. The initial profile of stars is shown as a dashed black line, while the present-day distribution of low mass stars (with uncertainties) from Schödel et al. (2018) is shown as a shaded region. *Bottom panel:* Density profiles of stars and compact objects in our Fiducial $\times 10$ model. For comparison, dash-dotted blue and green lines show, respectively the profiles of BHs and NSs, neglecting the pre-existing background of low mass stars/NSs (Fig. 1).

$2 \times 10^{-5} \text{ yr}^{-1}$ and $\dot{N}_{\text{ns}} = 4 \times 10^{-5} \text{ yr}^{-1}$, respectively (the old population of stars and their associated NSs are still neglected). The addition of NSs has little effect on the BH profile compared to the BH-only case. Outside of the injection radius, the slope of the NS density profile is similar to the BH one, but with a greater overall normalization reflecting the relatively higher NS injection rate. At radii $\lesssim r_i$, the BH density profile approaches the BW shape $n \propto r^{-7/4}$ (as in the BH-only case), while the NSs achieve a shallower profile $\propto r^{-3/2}$. A shallower profile for the lighter species

is expected for a two-component model in which the heavy species dominates the diffusion coefficients (Bahcall & Wolf 1977; Alexander & Hopman 2009).

The analytic arguments presented above are readily extended to the multi-species case. In particular, the BH density at r_i can again be estimated by replacing the single remnant mass m_c in eq. (7) with a weighted generalization

$$\tilde{m} = \left(\frac{\dot{N}_{\text{bh}} m_{\text{bh}}^2 + \dot{N}_{\text{ns}} m_{\text{ms}}^2}{\dot{N}_{\text{bh}} + \dot{N}_{\text{ns}}} \right)^{1/2}. \quad (11)$$

2.4 Effects of stellar background and potential

We now explore the effects of including the old population of low mass stars and NSs on the NSC evolution, the final step in constructing our models. Fig. 2 shows the profile of stars, NSs, and BHs at $t = 10$ Gyr in our Fiducial (top panel) and Fiducial $\times 10$ (bottom panel) models. BHs and NSs dominate the mass density inside of 0.03 (0.4) pc in the Fiducial (Fiducial $\times 10$) model.

The cusp of compact remnants causes the star cluster to expand radially over time, motivating our choice of a more compact initial stellar profile (black dashed line) than the currently-observed one (shaded gray region; Schödel et al. 2018). By contrast, the compact objects become slightly more centrally concentrated than in the previous models where the stars were neglected (Fig. 1). There are two reasons for this: (i) stars tend to scatter the higher mass compact objects to larger binding energies (ii) the gravitational potential of the stars suppresses outward diffusions of compact objects.

2.5 Non-fiducial NSC Models

This section explores other (“non-fiducial”) scenarios for creating the GC’s NSC, in which all of the stars and compact objects instead form as a single population with a common density profile and standard IMF. For one set of models, we assume all stars formed impulsively 10 Gyr ago. Such models allow us to compare our results to those of past work (e.g. Morris 1993; Miralda-Escudé & Gould 2000; Freitag et al. 2006), and are a useful limiting case if bursts of massive star formation occur with a $\gtrsim 100$ Myr cadence. We also consider models in which stars form at a constant rate with the present day observed profile. This model is unrealistic for the GC, but may be useful for other galactic nuclei with different star formation histories (Leigh et al. 2016). These models are summarized in Table 2.

Our models assume that stars are accreted in the distant past or form in-situ, neglecting on-going exchange of stars with the surrounding galaxy. We expect the exchange of low mass stars to be negligible as the energy relaxation time becomes longer than a Hubble time outside of a few parsecs. Ten solar mass BHs within ten parsecs of the center would sink to smaller radii within a Hubble time. Sinking from this scale would be captured by our impulsive models. On-going star cluster in-fall can bring additional stars to the center. However, the majority of the stellar mass brought in via globulars is accreted within ~ 1 Gyr (Arca-Sedda & Capuzzo-Dolcetta 2014; Gnedin et al. 2014).

Fig. 3 shows the BH profile at $t = 10$ Gyr which results if both stars and compact remnants are formed im-

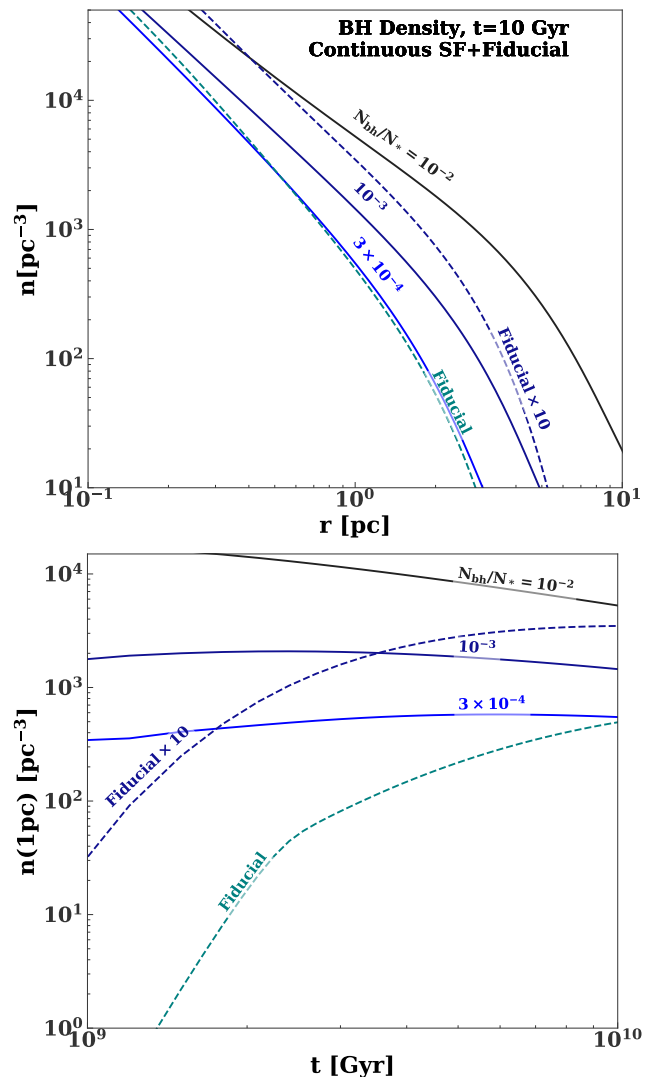


Figure 3. *Top panel:* Density profile of BHs at 10 Gyr for different star formation histories (Table 2). Solid lines show non-fiducial models in which the BHs form impulsively at $t = 0$ with the same profile as the stars (eq. 1), with colors labeling the ratio of BHs to stars. For comparison, dashed lines show our Fiducial and Fiducial $\times 10$ models, in which the BHs are instead injected continuously at small radii (see Fig. 2 and surrounding discussion). *Bottom panel:* Time evolution of the BH density at $r = 1$ pc for each of the formation histories shown in the top panel.

pulsively at $t = 0$ (initial scale radius of $r_o = 1$ pc) and assuming no subsequent star formation. We show results for a range of models which assume different ratios for the number of stars to compact objects, N_{bh}/N_{\star} . For a Kroupa IMF in which BHs originate from stars of mass $\gtrsim 25M_{\odot}$, we expect $N_{\text{bh}}/N_{\star} \sim 10^{-3}$, which (coincidentally) coincides with the number of BHs injected by the present day in our Fiducial $\times 10$ model. However, because the BHs in this case are injected directly at small radii, their density at radii $\lesssim 1$ pc in our Fiducial $\times 10$ models exceeds the primordial model with $N_{\text{bh}}/N_{\star} = 10^{-3}$ by a factor of a few.

Fig. 4 shows the BH density profile under the assumption that they form continuously at a constant rate over the

Table 2. Summary of models for assembling the populations of stars and compact remnants in the GC. The top two rows summarize our “fiducial” models, in which low mass stars and NSs are initialized at $t = 0$ following a radial profile given by eq. (1) with the scale radius r_0 and NS-to-star number ratio N_{ns}/N_{\star} . BHs and NSs are also continuously injected inside of ~ 0.3 pc, near the outer edge of the observed young stellar disks, with rates $\dot{N}_{\text{bh}}^{\star}$ and $\dot{N}_{\text{ns}}^{\star}$, respectively. The bottom three rows summarize other, non-fiducial scenarios, in which all compact remnants and stars form with the same radial distribution, either impulsively in the distant past or continuously. The masses of the stars, NSs, and BHs, are taken to be $0.3M_{\odot}$, $1.5M_{\odot}$, and $10M_{\odot}$, respectively.

| Scenario | r_o [pc] | $N_{\star}(t=0)$ | \dot{N}_{\star} [yr $^{-1}$] | $N_{\text{bh}}/N_{\star}(t=0)$ | $N_{\text{ns}}/N_{\star}(t=0)$ | $\dot{N}_{\text{bh}}^{\star}$ [yr $^{-1}$] | $\dot{N}_{\text{ns}}^{\star}/\dot{N}_{\text{bh}}^{\star}$ | M_{\bullet} | Fig. |
|--------------------------------|---------------|-------------------|------------------------------------|--------------------------------------|--------------------------------|--|---|---------------------------|------|
| Fiducial | 1.5 | 1.9×10^8 | 0 | 0 | 10^{-3} | 2×10^{-6} | 2 | $4 \times 10^6 M_{\odot}$ | 2 |
| Fiducial $\times 10$ | 0.5 | 1.9×10^8 | 0 | 0 | 10^{-3} | 2×10^{-5} | 2 | $4 \times 10^6 M_{\odot}$ | 2 |
| Impulsive | 1 | 1.9×10^8 | 0 | $3 \times 10^{-4}, 10^{-3}, 10^{-2}$ | $4N_{\text{bh}}/N_{\star}$ | 0 | – | $4 \times 10^6 M_{\odot}$ | 3 |
| Continuous SF Existing SMBH | 3 | 0 | 1.9×10^{-2} | $3 \times 10^{-4}, 10^{-3}, 10^{-2}$ | $4N_{\text{bh}}/N_{\star}$ | 0 | – | $4 \times 10^6 M_{\odot}$ | 4 |
| Continuous SF Growing SMBH | 3 | 0 | 1.9×10^{-2} | $3 \times 10^{-4}, 10^{-3}, 10^{-2}$ | $4N_{\text{bh}}/N_{\star}$ | 0 | – | 7% M_{tot} | 5 |

age of the NSC, with a spatial profile identical to the present-day stellar population. The BH density at small radii $\lesssim 1$ pc evolves significantly over time, taking several Gyr to reach a quasi-steady state.

Our previous scenarios assumed the central SMBH possesses a fixed mass, $4 \times 10^6 M_{\odot}$. However, if the NSC is built up by continuous star formation, then the SMBH may grow in concert with the cluster through gaseous accretion or star capture. Fig. 5 shows the density profiles of stars and compact objects at $t = 10$ Gyr if the SMBH mass is artificially fixed at all times to be 7% of the mass of the NSC. This speeds up the evolution because the velocity dispersion, and hence the cluster relaxation timescale (eq. 5) is smaller at early times. Nevertheless, the final distribution of BHs is similar to the previous cases (cf. Fig. 4).

Overall, we find that the final distribution of remnants after ~ 10 Gyr is mostly sensitive to the overall rate of production of BHs versus stars, and is rather insensitive to the details of the star formation history, or its precise radial distribution within the NSC.

2.6 Effects of strong scattering

So far we have neglected BHs ejecting stars via strong scatterings in our models. In this section we quantify this effect, which under some circumstances can be important for bulk cluster evolution (Lin & Tremaine 1980). The volumetric ejection rate at radius r is

$$\dot{n}_{\text{ej}}(r) = n_{\text{bh}}(r)n_{\star}(r)\langle\Sigma(v_{\infty})v_{\infty}\rangle \quad (12)$$

where $n_{\text{bh}}(r)$ is the number density of BHs, $n_{\star}(r)$ is the stellar density, v_{∞} is relative velocity at infinity, $\Sigma(v_{\infty})$ is the cross-section for ejection, and the angle brackets denote an average over the relative velocity distribution. This expression may be rewritten as

$$\dot{n}_{\text{ej}} = I(m_c/m_{\star})n_{\text{bh}}(r)n_{\star}(r)\sigma(r)\pi b_o^2$$

$$b_o = \frac{G(m_c + m_{\star})}{\sigma(r)^2} \quad (13)$$

where m_c and m_{\star} are the masses of the compact object and star respectively, $\sigma(r)$ is the (1D) velocity dispersion of the compact objects. The likelihood of ejection increases with the mass of the compact object, as quantified by the

dimensionless number I . In an encounter, the change in the star’s velocity is given by

$$\Delta v_{\parallel} = \frac{-2v_{\infty}}{1+x^2} \frac{m_c}{m_c + m_{\star}} \quad (14)$$

$$\Delta v_{\perp} = \frac{2v_{\infty}x}{1+x^2} \frac{m_c}{m_c + m_{\star}} \quad (15)$$

$$x = \frac{bv_{\infty}^2}{G(m_c + m_{\star})} \quad (16)$$

where the first and second lines are the components parallel and perpendicular to the initial relative velocity. The change in the star’s specific energy is

$$\Delta E = \frac{1}{2}\Delta v^2 + \Delta \mathbf{v} \cdot \mathbf{v}_{\star} \quad (17)$$

where \mathbf{v}_{\star} is the star’s initial velocity. For a star to be ejected ΔE should at least exceed the specific binding energy of the central SMBH, viz.

$$\Delta E \geq \frac{GM}{2r} = \frac{(1+\delta)}{2}\sigma(r)^2, \quad (18)$$

where δ is the logarithmic BH density slope. To determine the normalization of the ejection rate, we compute a Monte Carlo ensemble of encounters with different relative velocities, approach angles, and impact parameters. Assuming a Maxwellian velocity distribution for the stars and black holes, a uniform distribution of the cosine of the approach angle, and $\delta = 1.75$, the numerical pre-factor (I) in equation (13) is 0.1, 1, and 1.3 for $m_c/m_{\star} = 1, 10$, and 50 respectively (see also Henon 1969).

The total ejection rate may be dominated by stars on eccentric orbits. For a thermal eccentricity distribution and an $r^{-1.75}$ BH perturber profile, the ejection rate increases by a factor of ~ 3.7 (relative to purely circular orbits). Then, the ejection rate from strong scatterings is

$$\dot{n}_{\text{ej}} \approx 3.7\pi I(m_c/m_{\star})n_{\star}(r)n_{\text{bh}}(r)\sigma(r)^{-3}G^2m_c^2$$

$$\approx 4n_{\star}(r)\ln\Lambda^{-1}\tau_{\text{rx,bh}}(r)^{-1}, \quad (19)$$

where $\ln\Lambda \approx 15$ is the Coulomb logarithm and we take $m_c/m_{\star} = 10$. At any radius the time-scale for a star to be unbound from the central SMBH is approximately four times the local relaxation time of the BHs. To test how this effect would modify the stellar density, we add an additional sink term into PHASEFLOW. We find that the stellar density is modified by $\lesssim 25\%$ (40%) outside of 0.01 pc in our Fiducial (Fiducial $\times 10$) models. The total number of stars

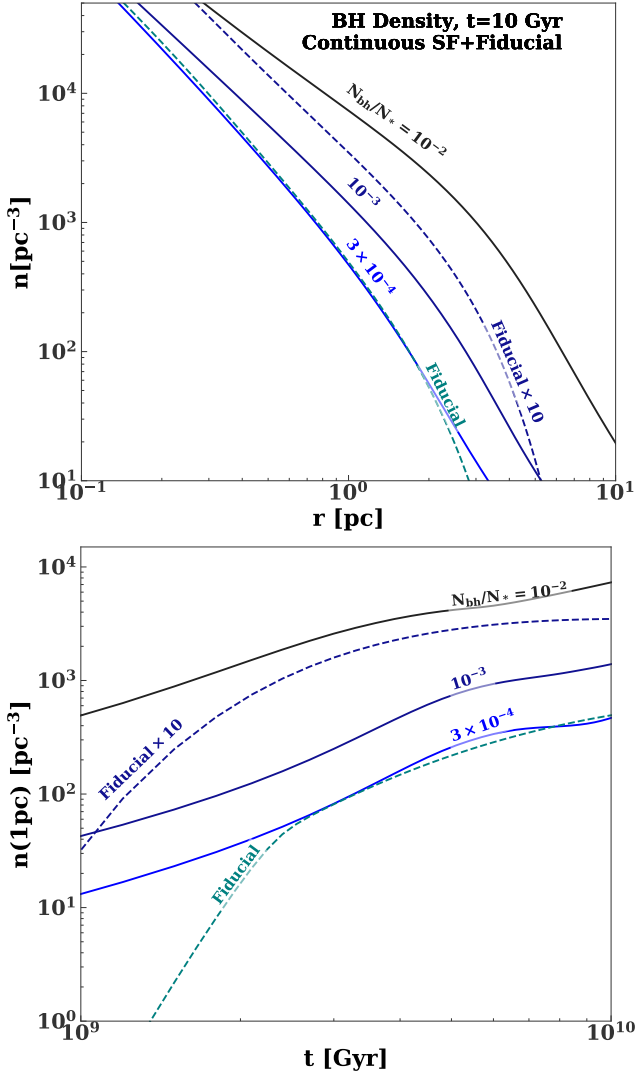


Figure 4. *Top panel:* Density profile of BHs at 10 Gyr under the assumption that the NSC is built up by continuous star formation at a constant rate with a spatial profile identical to the present-day stellar population; colors denote different ratios of BHs to stars, N_{bh}/N_{\star} . For comparison, dashed lines show the BH profile in our Fiducial and Fiducial×10 scenarios (Fig. 2). *Bottom panel:* Time evolution of the BH density at 1 pc, for each of the formation histories in the top panel.

ejected from the cusp is $\sim 2.7 \times 10^6$ in the Fiducial model and 7×10^6 in the Fiducial×10 model. These likely represent upper limits on the uncertainty caused by our neglect of strong scatterings, as Eq. 18 represents a generous ejection criterion.

3 TIDAL CAPTURE BINARY FORMATION

A close encounter between a star of mass m_{\star} and a compact object of mass m_c can lead to the formation of an XRB through tidal capture. During pericenter passage, tidal forces transfer orbital energy into stellar oscillations, capturing the star into an elliptical orbit.

The maximum initial pericenter distance that results

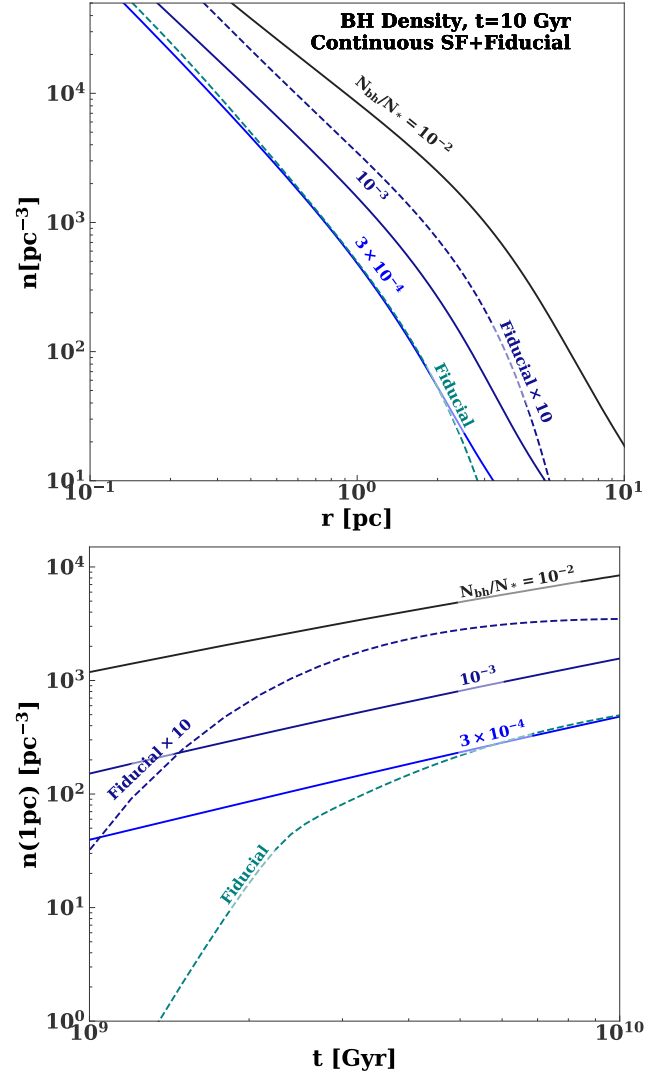


Figure 5. Same as Fig. 4, except the central SMBH is fixed to be 7% of the total cluster mass at all times, so that it grows with the cluster.

in tidal capture, r_{capt} , can be estimated by equating the hyperbolic orbital energy with the energy deposited in tides (see Appendix D of Stone et al. 2017b, and Appendix A in this paper). This condition can be expressed as

$$\mu \frac{v_{\infty}^2}{2} = \frac{Gm_{\star}^2}{r_{\star}} \left(\frac{m_c}{m_{\star}} \right)^2 \left(\frac{r_{\star}}{r_{\text{capt}}} \right)^6 T_2(r_{\text{capt}}, m_{\star}/m_c), \quad (20)$$

where r_{\star} is the stellar radius, μ is the reduced mass, and T_2 is the tidal coupling constant (we only include the dominant $l = 2$ modes, as even for an equal mass binary including the $l = 3$ modes only increases the maximum pericenter resulting in tidal capture by 5%). For distant pericenters this may be estimated using the linear theory (see Appendix A and Lee & Ostriker 1986). However, for the closest pericenters relevant for capture, linear theory underestimates the tidal coupling constant by a factor of a few. The magnitude of non-linear effects has been estimated for polytropic models

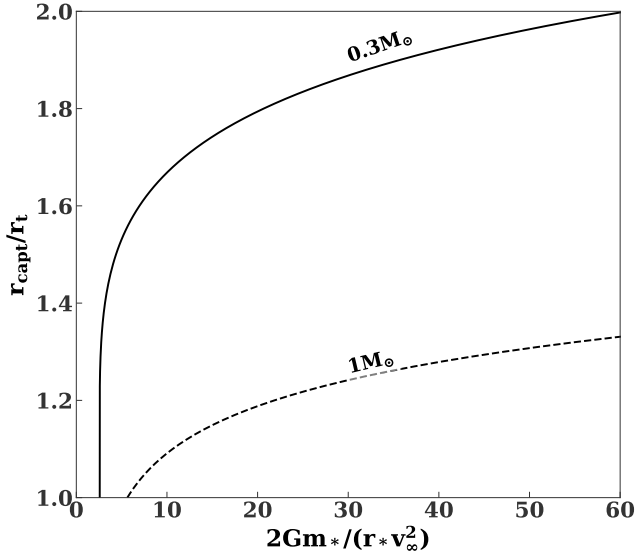


Figure 6. Maximum pericenter distance r_{capt} (normalized to the BH tidal radius r_t) at which a main sequence star can be tidally captured by a BH of mass $10M_\odot$, as a function of the stellar escape speed (normalized to the relative velocity at infinity, v_∞). Results are shown for two stellar masses, $0.3 M_\odot$ (solid line) and $1 M_\odot$ (dashed line). The former is modeled as an $n = 3/2$ polytrope and the latter is modeled as an $n = 3$ polytrope.

by Ivanov & Novikov (2001), and we adopt their prescriptions for close pericenters, as discussed in Appendix B.

Fig. 6 shows the maximum pericenter distance for tidal capture as a function of the relative velocity at infinity, v_∞ , normalized to the stellar escape speed, $v_{\text{esc}} = \sqrt{2Gm_*/r_*}$. The capture radius r_{capt} is typically $\lesssim 2$ times greater than the characteristic tidal radius $r_t \equiv r_*(m_c/m_*)^{1/3}$. Note that tidal capture cannot occur if $v_\infty \gtrsim v_{\text{esc}}$ and thus is suppressed at small radii $r \lesssim 0.1 - 1$ pc where the velocity dispersion is large; the same considerations virtually prohibit the tidal capture of giant stars in the GC. For even closer pericenter passages, inside of the so-called *disruption radius* $r_{\text{dis}} \approx 0.5 - 1.1r_t$ (depending on stellar structure; Guillochon & Ramirez-Ruiz 2013), stars are tidally disrupted rather than captured.

The combined volumetric rate of tidal captures ($r_{\text{dis}} \leq r_{\text{p}} \leq r_{\text{capt}}$) and disruptions ($r_{\text{p}} \leq r_{\text{dis}}$) at Galactocentric radius r is given by

$$\Gamma(r, t) = \int_0^{v_{\text{max}}(m_*)} n_c(r, t)n_*(r, t)v_\infty \pi r_o^2 \times \left[1 + \frac{2G(m_c + m_*)}{r_o v_\infty^2} \right] f(v_\infty, r, t) dv_\infty, \quad (21)$$

$$r_o = \max[r_{\text{capt}}(v_\infty, m_c/m_*), r_{\text{dis}}(m_*)]$$

where $n_c(r, t)$ is the number density of compact objects, $n_*(r, t)$ is the number density of stars, and $f(v_\infty)$ is the distribution of relative velocities. A hard upper limit to the value of $v_{\text{max}}(m_*)$ is the stellar escape velocity (for faster relative velocities most of star would remain unbound from the compact object in any tidal interaction), but in practice $v_{\text{max}}(m_*)$ is the relative velocity such that $r_{\text{capt}} = r_{\text{dis}}$ in eq. (20). This may be smaller than stellar escape speed by

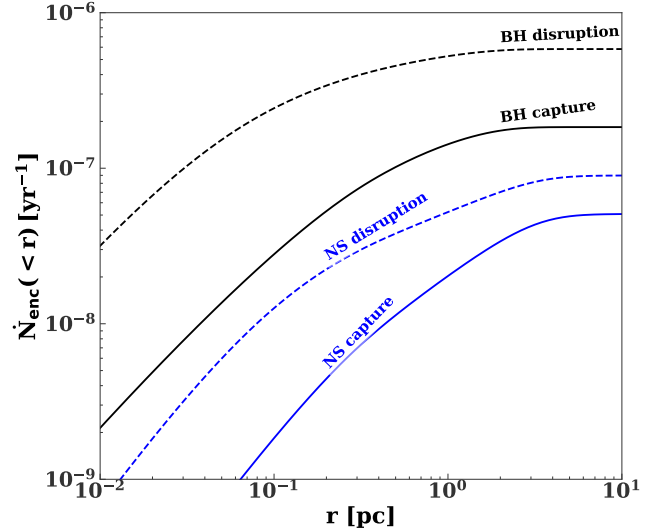


Figure 7. Present-day cumulative rate of tidal disruptions (dashed lines) and tidal captures (solid lines) inside of radius r for our Fiducial scenario. A total of $\approx 9 \times 10^{-7}$ strong tidal encounters occur per year.

a factor of ~ 2 . We approximate the velocity distribution as a Maxwellian, with a scale parameter equal to the local velocity dispersions of the two species added in quadrature.⁸ The term in brackets allows for gravitational focusing, which exceeds the geometric cross section for $r \gtrsim 0.01$ pc.

Fig. 7 shows our calculation of the present-day rate of total stellar tidal disruptions (dashed lines) and tidal captures (solid lines) by BHs and NSs, as calculated using the predictions of our Fiducial model for n_* and n_c . The capture/disruption rate by BHs exceeds that of NSs by a factor of $\gtrsim 3 - 10$ across most radii of interest; this is partially because in the limit of gravitationally-focused collisions, the rate of captures/disruptions obeys $\Gamma \propto m_c^{4/3}$. The rate of tidal captures is somewhat smaller than the rate of disruptions, since for typical relative velocities capture occurs over a narrower range of pericenter distance than does disruption. Some tidal captures may lead to a series of partial disruptions instead of the formation of a stable binary, even if the initial pericenter is outside of the disruption radius. Specifically, significant mass loss from the star is likely to lead to run-away heating that disrupts the star. In this paper we assume the star is eventually disrupted if it loses more than $\sim 10\%$ of its mass after its first pericenter passage (see the discussion in § 3.2).

Fig. 8 shows the tidal capture and disruption rate of stars by BHs as a function of time for different star formation histories corresponding to our Fiducial (§2.4) and non-fiducial scenarios (§2.5). In the Fiducial scenario, with compact remnant injection inside of ≈ 0.3 pc, the encounter rate increases for the first ~ 3 Gyr, as the number of compact objects increases. The rate then declines slightly as the com-

⁸ In detail the velocity distribution in the Keplerian potential of the SMBH is not Maxwellian, but this is a good approximation for our model stellar density profiles (see e.g. Alexander & Kumar 2001).

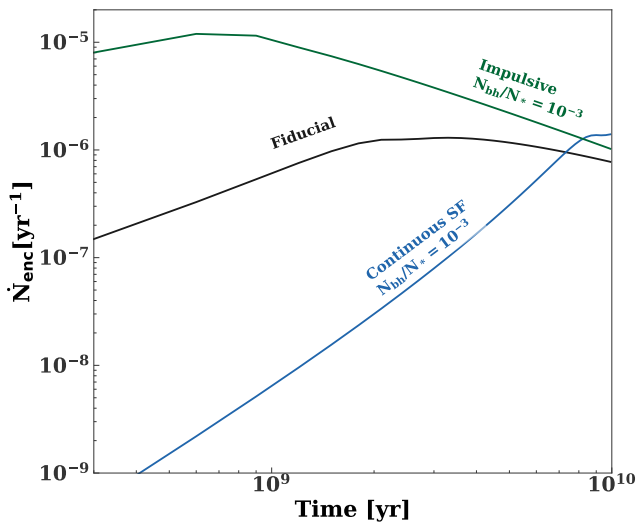


Figure 8. Rate of strong tidal encounters (disruptions plus captures) as a function of time in our Fiducial model (§ 2.4) as well as two of the non-fiducial scenarios (§ 2.5).

compact objects reach a steady state on small scales, while the population of pre-existing low mass stars are pushed outwards to larger radii. The non-fiducial scenario with impulsive injection of compact remnants and stars shows qualitatively similar behavior, but with the encounter rate peaking much earlier in time. Finally, in the non-fiducial scenario of continuous star formation, the encounter rate monotonically increases.

3.1 Tidal Capture and Circularization

As described by Stone et al. (2017b), there are three possible outcomes of a tidal capture: (1) the star continues to lose energy at each pericenter passage, until its orbit is circular; (2) the binary is perturbed by another star or compact object before circularization is complete; (3) the star inflates due to tidal heating, and is destroyed in a series of partial tidal disruptions.

Circularization of the binary can be interrupted (option 2) if the initial pericenter of the encounter is sufficiently large, in which case the tidal energy transfer is weak and the star barely captures into a highly elliptical orbit. In the limit of very large post-capture apocenter, an encounter with another star will perturb the orbital angular momentum faster than circularization can occur. Such encounters generally increase the angular momentum of the binary (since there is more phase volume at larger angular momenta), derailing the circularization process. However, comparing the time-scales for circularization and angular momentum diffusion (Stone et al. 2017b; their eqs. 21, 25), we find that circularization is slower than the outwards angular momentum diffusion time from stellar interactions for only a extremely narrow range of pericenters, within 10^{-3} of the maximum value for capture. Only a tiny fraction of tidally captured binaries will be perturbed by a third star before they circularize.

Another hazard for a tidally captured star is a string of partial disruptions due to the energy deposited by tides and

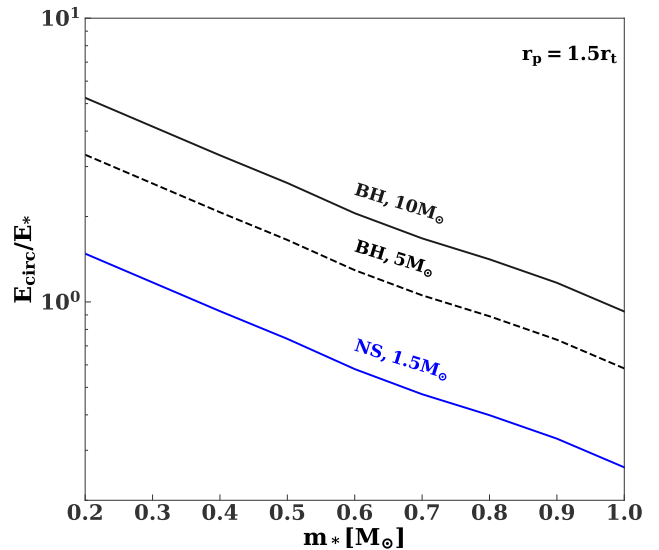


Figure 9. Ratio of the required to circularize the star into a binary with a NS or BH (E_{circ}) to the total (internal + gravitational binding) energy of the star (E_*) as a function of stellar mass. Although $E_{\text{circ}} \gtrsim E_*$ across much of the parameter space, tidal capture is not necessarily fatal for the star because the circularization energy can be deposited by modes primarily in the outer layers of the star, where it is likely to drive non-destructive mass loss.

tidal stripping near pericenter. Complete destruction of the star is energetically allowed if the energy released during circularization E_{circ} exceeds the total (internal + gravitational binding) energy of the star E_* . As shown in Fig. 9, a star captured by a black hole necessarily has $E_{\text{circ}} \gtrsim E_*$ (e.g. Kochanek 1992; Alexander & Morris 2003). The energy required for a star to circularize around a NS is smaller than the BH case, but still can be comparable to the energy of a low mass star.

However, even if $E_{\text{circ}} \gtrsim E_*$, this does not necessarily mean the star will be destroyed. If a significant fraction of the mode energy is thermalized near the stellar surface (e.g. as non-linear oscillations steepen into shocks), then it could be carried outwards in a super-Eddington wind (Fuller & Lai 2011, 2012; Wu 2018). Whatever remains of the star following this process would then still circularize, albeit with a lower mass and potentially higher entropy than its original state prior to being captured.

The star will lose mass during the circularization process (either due to mode dissipation or direct dynamical stripping at pericenter). The time-scale for mass loss is shorter than the thermal time-scale of the star and its radius will grow adiabatically (Linial & Sari 2017). As the star grows tidal dissipation becomes stronger, potentially leading to run-away heating and disruption of the star (Kochanek 1992). If the mass loss occurs primarily from the side of star closer to the compact object, the pericenter can grow faster than the stellar radius averting the run-away. However, this effect would only become important in nearly equal mass binaries in which the $l=3$ mode enhances (reduces) the displacement on the near (far) side of the star (Manukian et al. 2013).

Another important issue is the time-scale over which the mode energy deposited into the star is dissipated. [Mardling \(1995\)](#) has argued that a tidally captured star necessarily undergoes a random walk in eccentricity, since mode oscillations from consecutive pericenter passages would interfere with each other, leading to chaotic exchange of energy between the orbit and the star that would likely lead to the latter's disruption. However, this will not occur if the mode energy is dissipated over the course of a single orbit. This can plausibly occur via non-linear mode-mode couplings ([Kumar & Goodman 1996](#)), especially for the large amplitude modes that will be excited by tidal capture in the GC, where the energy deposited into the star on the first pericenter passage is $\gtrsim 10^{47}$ erg. For example, [Kumar & Goodman \(1996\)](#) show that the f -modes excited in low mass stars can dissipate energy on a time-scale of 30 ($E/10^{45}$ erg) days, where E is the energy deposited into the star. This would be shorter than the orbital period of a captured low mass star ($\gtrsim 5$ days). Higher mass stars can dissipate energy even more efficiently by resonantly exciting g-modes, and nonlinear oscillations may dissipate their energy even faster by steepening into shocks.

The long-term evolution of a highly eccentric tidal capture binary remains an open question, and its solution is beyond the scope of this work. For the remainder of this paper, we assume that tidal capture binaries are in fact able to circularize without being destroyed, so long as no more than 10% of the star's mass is lost on the first pericenter passage, but this assumption must be examined in future modeling.

3.2 X-ray Binary Formation and Evolution

Once the star circularizes into an orbit around the compact object, the binary semi-major axis a will be roughly twice the pericenter radius of the captured star.⁹ The orbit will then decay over long timescales due to gravitational wave emission¹⁰, such that a decreases according to

$$\frac{\dot{a}}{a} = 2 \frac{\dot{J}_{\text{GW}}}{J} = -\frac{64}{5} \frac{G^3}{c^5} \frac{m_* m_c (m_* + m_c)}{a^4}. \quad (22)$$

Here J is the circular orbit angular momentum, and \dot{J}_{GW} is the quadrupole-order rate of angular momentum radiation ([Peters 1964](#)). Once the system enters Roche-lobe contact, the subsequent evolution of the semi-major axis and mass accretion rate onto the compact object obey (e.g. [Frank et al.](#)

⁹ The relation $a = 2r_p$ will be exact if angular momentum and mass are conserved during circularization, except for a correction for stellar spin ([Lee & Ostriker 1986](#)).

¹⁰ In principle spin-down by magnetic braking also contributes to angular momentum losses from the star. However, there is considerable uncertainty in the spin-down rate for high rotation speeds in contact binaries. Empirically, magnetic braking is sub-dominant to gravitational wave emission in BH binaries, as otherwise one predicts a population of bright, persistent short period BH LMXBs that are not observed (see [Yungelson et al. 2006](#); [Ivanova & Kalogera 2006](#)). By analogy with cataclysmic variables, magnetic braking is likely also sub-dominant in NS systems with periods $\lesssim 3$ hours.

2002)

$$\begin{aligned} \frac{\dot{m}_*}{m_*} &= \frac{\dot{J}_{\text{GW}}}{J} \left[1.2 - \frac{m_*}{m_c} \right]^{-1} \\ \frac{\dot{a}}{a} &= 2 \frac{\dot{J}_{\text{GW}}}{J} - 2 \frac{\dot{m}_*}{m_*} \left(1 - \frac{m_*}{m_c} \right), \end{aligned} \quad (23)$$

where we have assumed the star maintains thermal equilibrium, i.e. that its radius follows the main-sequence, $r_* \propto m_*^{0.8}$.

[Fig. 10](#) shows the binary lifetime after the star enters Roche-Lobe contact as a function of the masses of the star and compact remnant. The lifetime is defined as the interval over which (1) the star has not yet evolved off the main sequence and (2) the star's mass still exceeds $0.1M_\odot$. The last condition is motivated by the fact that once $m_* \lesssim 0.1M_\odot$ the star's equation of state changes, resulting in a one to two order of magnitude reduction in the mass-transfer rate (and an undetectably dim X-ray source). Likewise, if the star evolves off the main sequence, the star and compact object may undergo a common envelope phase, with an outcome that is uncertain theoretically.

[Fig. 10](#) shows that the binary lifetime decreases for larger compact object masses, due to more rapid evolution through gravitational wave emission. For low-mass stars ($m_* \lesssim 1M_\odot$), the binary lifetime also increases with m_* because the tidal radius (and thus the initial separation) is larger for higher mass stars. For massive stars ($m_* \gtrsim 1M_\odot$), the binary lifetime is instead limited by the main-sequence lifetime.

The present-day ($t = t_h = 10$ Gyr) density of XRBs at radius r is approximately given by¹¹

$$n_x(r) = \int_0^{t_h} \int_{r_{\text{min}}(t)}^{r_{\text{max}}(t)} d\Gamma(r_p, r, t) dr_p dt, \quad (24)$$

where

$$\begin{aligned} d\Gamma(r_p, r, t) &= n_c(r, t) n_*(r, t) \sigma 2\pi r_p \times \\ &\left[I_0(r_p, \sigma) + \frac{G(m_c + m_*)}{\sigma^2 r_p} I_1(r_p, \sigma) \right] \\ I_0(r_p, \sigma) &= \int_0^{v_\infty(r_p)} \frac{v_\infty}{\sigma} f(v_\infty) dv_\infty \\ I_1(r_p, \sigma) &= \int_0^{v_\infty(r_p)} \frac{\sigma}{v_\infty} f(v_\infty) dv_\infty, \end{aligned} \quad (25)$$

is the capture rate per unit pericenter, $v_\infty(r_p)$ is the maximum relative velocity that would result in a capture (the second term in the brackets dominates). The limits of integration in eq. 24 are the minimum and maximum initial pericenters for which the binary would be active today.

For close pericenters, the star loses a significant fraction of its mass via direct tidal stripping, leading to the star's destruction in a series of partial disruptions. Quantitatively, [Ivanov & Novikov \(2001\)](#) find that an $n = 3/2$ (3) polytrope would lose 10% of its mass for a pericenter of 1.5 (1) r_t .

¹¹ Eq. (24) implicitly assumes that binaries are visible as XRB at the radii where they are formed. In reality, binaries radially diffuse over time after forming, an effect we quantify in [Fig. 12](#).

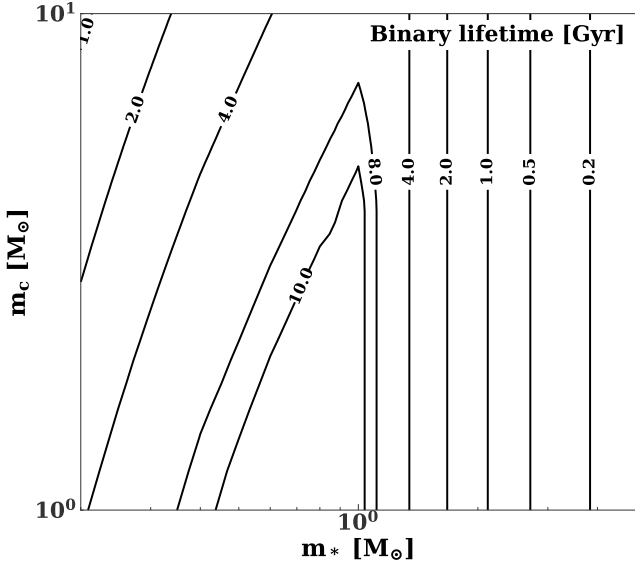


Figure 10. Binary lifetime after Roche-Lobe contact is reached as a function of the stellar mass (m_*) and compact object mass (m_c). The binary lifetime is defined as the interval over which the following criteria are met: (1) the companion mass still exceeds $0.1 M_\odot$ and (2) the star has not evolved off the main sequence. We use equation 5 from Hurley et al. (2000) for the main sequence lifetime (and assume a solar metallicity star).

Based on these results we also require

$$r_p > \begin{cases} 1.5r_t, & m_* \leq 0.7M_\odot \\ r_t, & m_* > 0.7M_\odot \end{cases}. \quad (26)$$

Modern hydrodynamic simulations (Mainetti et al. 2017) find comparable results with ten percent mass loss at $r_p/r_t \approx 1.6$ ($r_p/r_t \approx 0.95$) for $n=3/2$ ($n=3$) polytropes. As we use the tidal coupling constants from Ivanov & Novikov (2001), we also use their prescription for stellar mass loss.

To accurately calculate the tidal capture rate at small Galactocentric radii (where the rate becomes zero for stellar velocities equal to the local velocity dispersion σ), we must integrate over the velocity distribution. For a Maxwellian velocity distribution, the integrals over relative velocity in eq. (25) can be evaluated analytically:

$$I_0(r_p, \sigma) = \sqrt{\frac{2}{\pi}} \left[e^{-\frac{v_\infty(r_p)^2}{2\sigma^2}} \left(-\frac{v_\infty(r_p)^2}{\sigma^2} - 2 \right) + 2 \right]$$

$$I_1(r_p, \sigma) = \sqrt{\frac{2}{\pi}} \left(1 - e^{-v_\infty(r_p)^2/2\sigma^2} \right). \quad (27)$$

Fig. 11 shows our calculation of the cumulative tidal capture rate inside radius r , using our Fiducial model for the time-dependent density profiles of BHs, NSs, and stars (Fig. 2). We explore the dependence of the capture rate on stellar mass by fixing the number density of the stars, but varying their mass m_* . The *per star* capture rate is larger for higher mass stars due to their larger tidal radii; however, lower mass stars are more numerous for any realistic mass function and thus dominate the total number of formed binaries.

Fig. 12 shows our fiducial model predictions for the present-day total number of accreting BH and NS XRBs in-

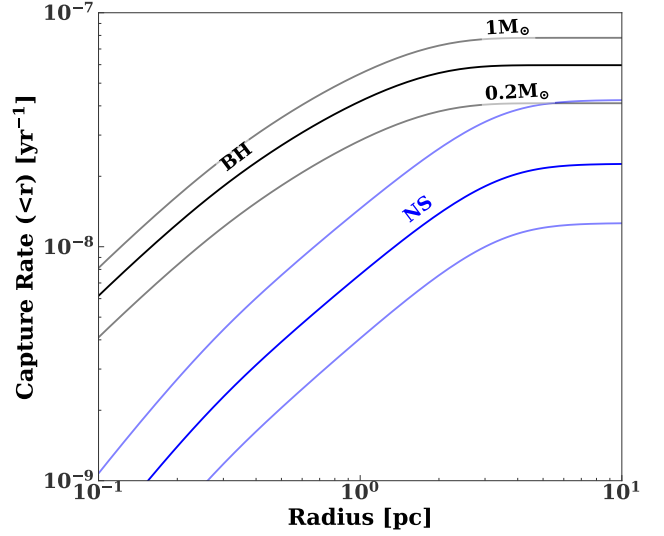


Figure 11. Present-day binary formation rate from tidal captures of low mass stars by BHs (black lines) and NSs (blue lines) interior to a given Galactocentric radius r , as calculated using our Fiducial model for the population of stars and compact remnants in the GC (Fig. 2). The thin lines show models in which we have fixed the stellar density but consider a single-mass population of stars with $m_* = 0.2M_\odot$ or $1M_\odot$. The thick lines show the capture rate assuming a more realistic Kroupa mass function which extends from $0.2 - 1 M_\odot$.

terior to a given radius. Dashed lines show the initial radial distribution of the binaries just after forming, while solid lines show the distribution, allowing for relaxation within the cluster potential. To calculate the latter, we first find the PHASEFLOW snapshot with a look-back time equal to the mean binary lifetime. Then, we insert a “tracer” population of binaries with the expected initial distribution, and evolve the system forward in time.

Table 3 summarizes the predictions of our fiducial models for the number of tidally-captured XRBs in the central parsec of our GC. The average accretion rate for BH (NS) binaries is 10^{-10} (3×10^{-11}) $M_\odot \text{ yr}^{-1}$, corresponding to 5×10^{-4} (10^{-3}) of the Eddington rate $\dot{M}_{\text{Edd}} = L_{\text{Edd}}/0.1c^2$, where $L_{\text{Edd}} = 1.3 \times 10^{38} (m_c/M_\odot) \text{ erg s}^{-1}$ is the Eddington luminosity. These accretion rates are generally less than the theoretical critical threshold value below which the disk is thermally unstable,

$$\dot{M}_{\text{crit}} \approx 3.2 \times 10^{-11} M_\odot \text{ yr}^{-1} \left(\frac{m_c}{M_\odot} \right)^{0.5} \left(\frac{m_*}{M_\odot} \right)^{-0.2} \times \left(\frac{P}{1 \text{ hour}} \right)^{1.4}, \quad (28)$$

where m_c , m_* , and P are the mass of the compact object, mass of the donor star, and period of the orbit, respectively (Dubus et al. 1999). Thus, we expect XRBs formed by tidal capture to be transient sources, with long quiescent periods interspersed with bright outbursts.

4 X-RAY OBSERVATIONS

Hailey et al. (2018) discovered twelve new non-thermal X-

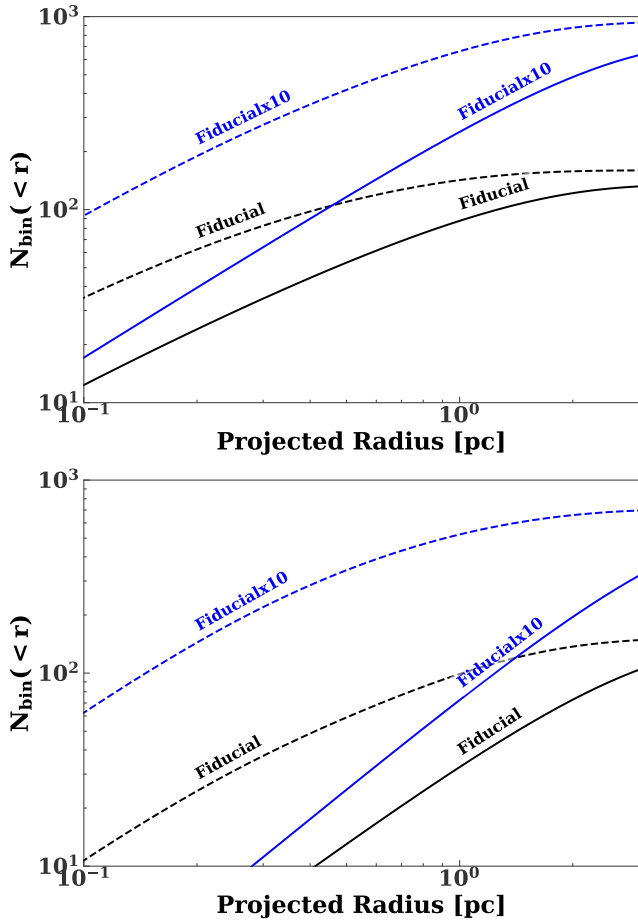


Figure 12. Cumulative number of tidal capture BH-XRB (top panel) and NS-XRB (bottom panel) predicted inside Galactocentric radius r for our Fiducial and Fiducial \times 10 scenarios. Dashed lines show the distribution of initially- formed binaries, while solid lines show the final distribution after allowing for dynamical relaxation of the binary population (these are calculated by inserting a tracer population with formed distribution of the binaries into the model snapshot corresponding the mean binary age).

ray sources in the central parsec of our galaxy. Of these, six are solid BH-XRB candidates, while the identity of the remainder is less certain (they may be either additional XRBs or MSPs). In principle, many more sources may be present with luminosities below the *Chandra* detection threshold of $L_x \approx 4 \times 10^{31}$ erg s $^{-1}$. Indeed, field BH-XRBs are known with luminosities as low as $L_x \approx 2 \times 10^{30}$ erg s $^{-1}$ (Armas Padilla et al. 2014). To estimate the total number of unobserved XRBs lurking in the central parsec, Hailey et al. (2018) first estimate what the flux of the minimum luminosity source from Armas Padilla et al. (2014) would be if it were in the GC (accounting for absorption and instrumental response). Then, extrapolating the field luminosity function ($N(> F) \propto F^{-\alpha}$, $\alpha = 1.4 \pm 0.1$) to this flux, they conclude that the total number of XRBs could be as high as 300–1000.

4.1 Comparison to Tidal Capture Model

For our fiducial models, we predict a total of 60–200 BH XRBs, which is comparable to the total number inferred from observations (Table 3). These numbers would require the luminosity function to extend a factor of $\sim 3–15$ below the detection threshold. Fig. 13 shows that cumulative radial distribution of XRBs from our models at radii $\gtrsim 0.2$ pc also agrees well with the distribution measured by Hailey et al. (2018). (We only consider binaries outside of 0.2 pc, as observational limits prevent the identification of individual sources inside this radius). Specifically, we predict average XRB surface density profiles $\Sigma \propto r^{-1.4}$ and $\propto r^{-0.9}$ in our Fiducial and Fiducial \times 10 models, respectively. These slopes are close to the measured surface density profile of high S/N sources: $\Sigma \propto r^{-1.5 \pm 0.3}$ in the radial range $0.2 \text{ pc} \lesssim r \lesssim 1 \text{ pc}$ (Hailey et al. 2018). There are no strong detections (> 100 counts) outside of the central parsec, but there are an additional 40 lower significance detections (> 50) counts between 1 and 3.5 pc (though some of these may be due background contamination).

The numbers we give assume that the stars lose a small fraction of their mass as their orbits circularize. As previously discussed, the final outcome of this process is uncertain, and it is possible that some stars may be completely destroyed. Alternatively, some stars may lose an order unity fraction of their mass even if they are not destroyed. We re-did our calculations, assuming that every star loses half of its mass in the circularization process. The number of BH-XRBs is reduced by a factor of three under this assumption.

4.2 Neutron Stars

The number of NS-XRBs formed in the central parsec for our Fiducial and Fiducial \times 10 models are $N_{\text{ns}} \approx 30$ and ≈ 70 , respectively. These numbers, which are a factor of $\approx 2–3$ times lower than the predicted number of tidal capture BH-XRBs in this region, and significantly exceed the ≤ 3 NS-XRBs observed thus far.

What might suppress the NS population? First, as in the BH case, not all NS binaries manifest as luminous XRBs. Furthermore, some NS-XRBs may evolve into millisecond pulsars later in their evolution. Only 3% of the known population of MSP have properties which would make them detectable in the GC (Perez et al. 2015); given that up to six of the observed X-ray sources in the central parsec could be MSPs, as many as ~ 200 MSPs could exist in this region.

The relative number of tidally captured BHs versus NSs binaries also depends on the fate of massive stars. Although we have assumed that stars of ZAMS mass $\gtrsim 25M_{\odot}$ become BHs, in reality there is not a single mass separating BH and NS progenitors (Sukhbold et al. 2016), and the fraction of O/B stars that evolve into NSs (as opposed to BHs) may differ between the field and the GC.

The NS population could also be reduced by supernova kicks, which would eject $\sim 40\%$ of isolated NS formed in the central disk for a Maxwellian kick velocity distribution, with $\sigma = 265 \text{ km s}^{-1}$ (Hobbs et al. 2005). However, $\sim 40\%$ (10%) of the NS binaries in our Fiducial (Fiducial \times 10) model come from NSs associated with the old stellar population, calibrated to the Ivanova et al. (2008) model of globular clusters (and this already accounts for supernova kicks). Overall

Table 3. Number of tidally-captured BH- and NS-XRBs in the GC predicted for our fiducial scenarios as compared to the observed population. The “Observed” XRBs corresponds to the population detected by Hailey et al. (2018), while the “Extrapolated” sources account for an (uncertain) extrapolation of the X-ray luminosity function below the *Chandra* detection threshold (see text for details).

| Scenario | BH-XRB ($r \leq 1$ pc) | BH-XRB ($r \leq 3.5$ pc) | NS-XRB ($r \leq 1$ pc) | NS-XRB ($r \leq 3.5$ pc) |
|--------------|----------------------------|------------------------------|--------------------------------|----------------------------------|
| Fiducial | 64 | 110 | 29 | 110 |
| Fiducialx10 | 210 | 640 | 67 | 370 |
| Observed | 6–12 | $\lesssim 50$ | 1–3 (LMXB), $\lesssim 6$ (MSP) | 3–6 (LMXBs), $\lesssim 50$ (MSP) |
| Extrapolated | 300–1000 | | $\lesssim 200$ (MSP) | $\lesssim 1000$ (MSP) |

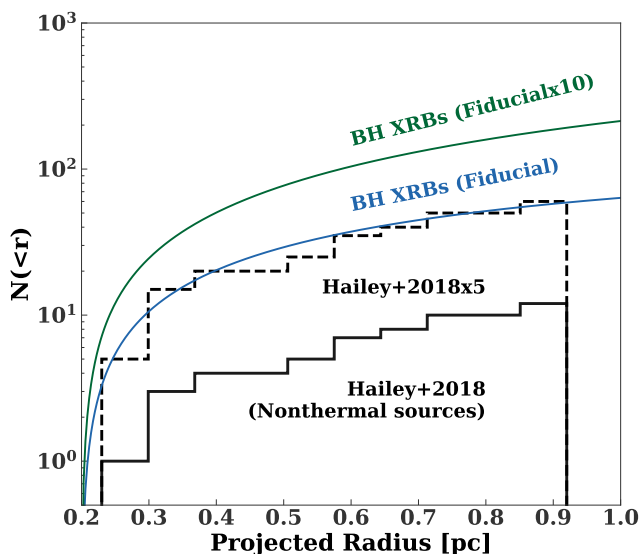


Figure 13. Cumulative number of BH XRBs inside projected Galactocentric radius r from our fiducial models compared with the non-thermal sources identified by Hailey et al. (2018) (solid black line). We have included the six sources that may be MSPs instead of BH-XRBs in the latter. The dashed black line shows the distribution of sources scaled up to match the normalization of the Fiducial model. The region inside of 0.2 pc is not included as the population of non-thermal sources is not observationally constrained there.

supernova kicks would reduce the number of neutron star binaries by $\sim 25\%$ ($\sim 40\%$) in our Fiducial (Fiducial $\times 10$) model.

Finally, we note the population of NS XRBs is more sensitive to the initial conditions than BH XRBs. The progenitors of NS XRBs in our models typically formed ~ 7 –8 Gyr ago (in comparison to ~ 4 Gyr ago for BH XRBs). The cluster expands over time, so our models assume the NSC was initially more compact than it is today. However, a small uncertainty in the present day density translates into a large uncertainty in the initial density. We redid our calculation for the number of NS XRBs holding the stellar density fixed to the present day profile. We find that the number of NS XRBs is reduced by a factor of ~ 2 , while the number of BH XRBs is only reduced by 30%.

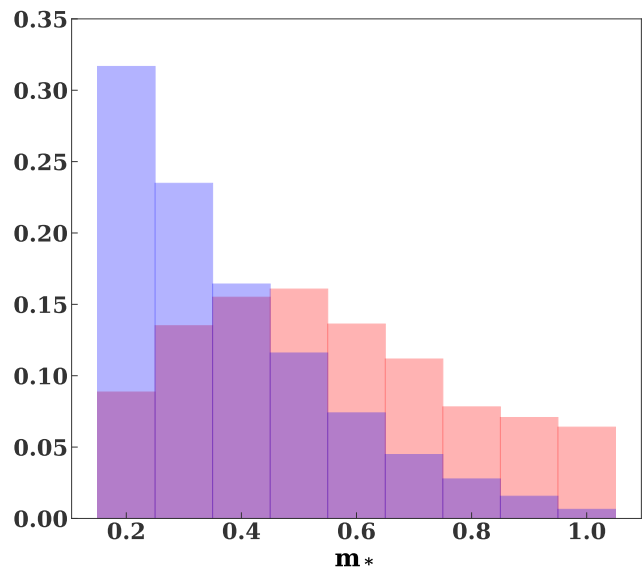


Figure 14. Histogram of companion masses of present-day BH XRBs (blue) and companion masses of their progenitors (red). The difference between the final and initial masses is due entirely to post-circularization Roche-Lobe overflow accretion; additional mass may be lost during the circularization process itself.

5 PREDICTIONS AND IMPLICATIONS OF OUR MODELS

In this section we summarize various implications of our models, including properties of binaries and rates of various electromagnetic transients (including tidal disruption events and stellar collisions). We also estimate the formation rate of BH-BH binaries due to bound-free gravitational wave emission. Table 4 summarizes the rates of these processes in our GC models.

5.1 Properties of binaries

XRBs formed by tidal capture are necessarily short period systems. The binaries in our models have main sequence companions with periods of $\lesssim 10$ hours (with a median period of ~ 3.6 hours). Any future periodicity identified in the quiescent population would be a powerful discriminant between tidal capture and other channels (e.g. binary exchange) that can form long period XRBs. We show a histogram of the companion masses of present day BH XRBs in our Fiducial model in Fig. 14.

In the field such short-period XRBs possess low lumi-

nosities of $\lesssim 10^{31}$ erg s $^{-1}$ (Armas Padilla et al. 2014) which are below the detection threshold of Hailey et al. (2018) and thus could not be contributing to the observed population. However, the current sample of short period BH-XRBs is small (only four are known with a period of less than six hours).

5.2 Tidal disruptions by the central SMBH

Stars may also be tidally disrupted by the central SMBH (Hills 1975). Such tidal disruption events (TDEs) can produce bright electromagnetic flares (Rees 1988). Many candidate flares have now been detected in optical/UV (Gezari et al. 2006, 2008; van Velzen et al. 2011; Gezari et al. 2012; Chornock et al. 2014; Holoien et al. 2014; Arcavi et al. 2014; Vinkó et al. 2015; Holoien et al. 2016b,a; Blagorodnova et al. 2017), and X-ray wavelengths (see Auchettl et al. 2017 and the references therein).

The total TDE rate due to two-body relaxation has been estimated for a large *Hubble Space Telescope* (*HST*) sample of nearby galactic nuclei (Wang & Merritt 2004; Stone & Metzger 2016). These authors find that the average per-galaxy disruption rate is $\sim 1 - 10 \times 10^{-4}$ per year. This range appears discrepant with observationally inferred TDE rate estimates, which are often $\sim 10^{-5}$ galaxy $^{-1}$ yr $^{-1}$ (Donley et al. 2002; van Velzen & Farrar 2014). While recent work has suggested that properly accounting for the broad TDE luminosity function (van Velzen 2018) may bring observational TDE rates into agreement with theory, it is worth considering one limitation of the theoretical estimates: in the smallest galaxies, even *HST* observations underresolve the SMBH influence radius (from which most TDEs are sourced), and moderate inward extrapolation is needed to calibrate theoretical models (Stone & Metzger 2016). The TDE rates predicted by our Fokker-Planck models have been calibrated off scales far smaller than the Sgr A * influence radius, and are thus a useful sanity check on TDE rate calculations in general.

Fig. 15 shows the TDE rate for a few different models for the GC. The present-day TDE rate in each is $\sim 10^{-4}$ stars per year ($3 \times 10^{-5} M_{\odot}$ yr $^{-1}$), similar to previous theoretical estimates for SMBHs of similar size (Wang & Merritt 2004; Stone & Metzger 2016). Unsurprisingly, the *present-day* disruption rate is similar for different models as they are all tuned to reproduce the present-day observed stellar density profile. However, different star formation histories lead to very different temporal behavior in TDE rates (see also Aharon et al. 2016). In our models of the GC (Fiducial and Fiducial $\times 10$), all of the lower main sequence stars formed impulsively in the distant past, and the star cluster expands over time. Therefore, the TDE rate decreases at late times. In contrast, the TDE rate monotonically increases in a galactic nucleus that is continuously forming stars (see the dashed grey line in Fig. 15).

Our current sample of (thermal) TDEs is limited to the low-redshift universe, but *LSST* and *eROSITA* are expected to find TDEs out to $z \approx 1$. The rates of high- z tidal disruption that these surveys find will therefore carry information

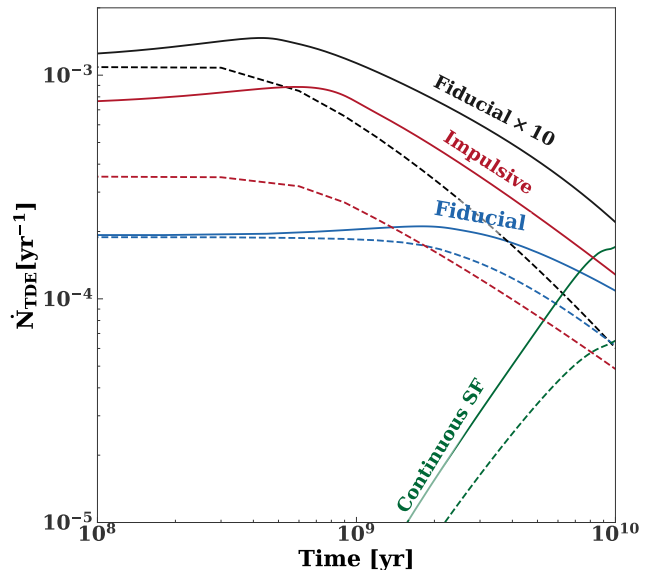


Figure 15. Rate of tidal disruption by the central SMBH as a function of time for our GC models (Fiducial and Fiducial $\times 10$). We also show hypothetical models with continuous star formation (green line), and a single population formed 10^{10} years ago (red lines) (see § 2.5). The dashed lines show what the disruption rate would be without stellar mass BHs (calculated by excluding the compact objects from the angular momentum diffusion coefficients).

on the growth history of nuclear star clusters (Aharon et al. 2016).¹²

The SMBH can accumulate a substantial fraction of its mass by disrupting stars and accreting compact objects. After a TDE, half of the disrupted star is bound to the SMBH. If the SMBH consumed half of each disrupted star it would grow by 3×10^5 (1.4×10^6) M_{\odot} ($\sim 8-40\%$ of its present day mass). However, a significant fraction of the initially bound debris may be lost in outflows, so the mass accreted may be $\lesssim 10\%$ of the disrupted star’s mass (Metzger & Stone 2016). If the SMBH accretes ten percent of each disrupted star it would grow by 10^5 (8×10^5) M_{\odot} . In the last case, most of this mass ($5 \times 10^5 M_{\odot}$) comes from consumption of compact objects. For simplicity, we fix the mass of the SMBH to $4 \times 10^6 M_{\odot}$ in our fiducial models.

5.3 Tidal disruptions by stellar mass compact objects

Stars that enter the tidal radius of a stellar compact object are also tidally disrupted, powering a transient flare of electromagnetic emission. We calculate the total rate of such “micro-TDEs” in our Fiducial model to be $\sim 6 \times 10^{-7}$ per year (see Fig. 7). Thus, the micro-TDE rate in the GC is comparable to the rate from globular clusters, perturbations of wide binaries in the field, and disruptions induced by natal kicks (Perets et al. 2016). Because the resulting flare is short-lived (Perets et al. 2016 estimate the the viscous

¹² Although other factors, such as the evolution of the SMBH mass function, will also contribute - see e.g. Kochanek 2016).

time-scale of the debris to be less than a day), it is highly unlikely any such disruption events would be observable in our own GC today. However, such events in other galactic nuclei might produce rare short-lived transients detectable at cosmological distances - for example, “ultra long” gamma ray bursts (GRBs; [Levan et al. 2014](#)). Taking into account selection effects, the total rate ultra-long GRBs may be comparable to the rate of classic long GRBs: $\sim 10^{-6}$ per galaxy per year (at $z = 0$) after beaming corrections ([Guetta et al. 2005](#)). Interestingly, this is comparable to the micro-TDE rate. However, we note that ultra long GRBs can also be explained by the core collapse of massive stars ([Greiner et al. 2015](#)).

At very small Galactocentric radii, these micro-TDEs may occur without producing observable accretion flares. This will occur if the relative velocity v_∞ between the star and the compact object is too large for any of the tidal debris to remain bound, i.e. if $v_\infty^2/2 > (m_c/m_\star)^{1/3} Gm_\star/r_\star$ ([Hayasaki et al. 2018](#)). We have excluded such hyperbolic micro-TDEs from our rate estimates.

The small mass ratio between NSs and main sequence stars means that many “micro-TDEs” involving NSs will actually be direct physical collisions, where a Thorne-Zytkow object may be formed (although the stability of such objects remains uncertain).

5.4 Red giant depletion

As pointed out by [Genzel et al. \(1996\)](#), there is a dearth of bright red giants ($K < 10.5$) within ~ 0.2 pc of the GC. There is a similar dearth of intermediate luminosity ($10.5 < K < 12$) giants within ~ 0.08 pc. The distribution of fainter stars, on the other hand, is smooth, and has no holes on small scales.

It has been suggested that collisions of red giants with main sequence stars and BHs ([Dale et al. 2009](#), D09 hereafter) could cause the observed holes in the red giant population. D09 find that stripping is only effective in reducing the brightness of giants in the RGB phase (and has little effect on AGB and horizontal branch stars). Furthermore, only close pericenters ($r_p \lesssim 15R_\odot$ for a solar type giant) will remove enough material to significantly alter the evolution of the giant (see also [Leigh et al. 2016](#)). They conclude that 2×10^4 BHs inside of 0.1 pc are required to explain the observed dearth of intermediate luminosity giants. The gap in the bright giants is harder to explain, as it would require even larger numbers of BHs that would make the gap in the intermediate luminosity giants too large.

In our Fiducial (Fiducial $\times 10$) model the number of BHs inside 0.1 pc is 1200 (3600), much smaller than the number required to explain the depleted giants. The intermediate luminosity giants are ~ 2 -3 solar mass stars that spend $\lesssim 100$ Myr on the red giant branch. The time-scale for close encounters only becomes comparable to the giant lifetime inside of ~ 0.01 pc. We conclude that it is difficult to account for the depletion of red giants by collisions with BHs alone. However, there are many alternative explanations for the dearth of red giants in the literature. For example, red giants may be destroyed by collision with a clumpy gas disk ([Amaro-Seoane & Chen 2014](#); [Kieffer & Bogdanović 2016](#)).

Ordinary stars may also collide with each other. We

calculate the present-day rate of star-star collisions outside of 0.1 pc to be 7×10^{-6} per year.

5.5 Two body BH-BH binary formation

Close encounters between BHs can result in the formation of close binaries, either via three-body interactions or two-body gravitational wave bound-free emission ([Antonini & Rasio 2016](#)). GW capture is generally sub-dominant to three-body processes, but it is one of the few ways to produce LIGO sources with a non-negligible eccentricity. All else being equal, eccentric sources are louder and would be detectable to larger distances. Additionally, eccentric sources can sometimes provide more stringent tests of strong field gravity, as a larger fraction of the energy is emitted when the source is moving at high velocities ([Loutrel et al. 2014](#)). The maximum impact parameter that results in binary formation is

$$b_{\text{gw}} = \left(\frac{340\pi}{3} \right)^{1/7} \frac{Gm_{\text{tot}}}{c^2} \eta^{1/7} \left(\frac{v_\infty}{c} \right)^{-9/7}$$

$$\eta = \frac{m_1 m_2}{(m_1 + m_2)^2}, \quad (29)$$

as in equation 17 of [O’Leary et al. \(2009\)](#). The total rate of GW captures in our Fiducial (Fiducial $\times 10$) model is $\sim 10^{-10} \text{ yr}^{-1}$ (10^{-9} yr^{-1} ; see also Table 4), within the range of estimates from [O’Leary et al. \(2009\)](#).

An estimate of the total rate of double compact object binary formation, including three-body processes, is beyond the scope of this paper, and we leave this to future work.

6 SUMMARY AND CONCLUSIONS

[Hailey et al. \(2018\)](#) have recently identified 6-12 quiescent BH-LMXB candidates within one parsec of the Galactic Center, and infer that there may be hundreds of fainter systems in the same region. This means that the GC is three orders of magnitude more efficient than the field at producing BH-XRBs, recalling the analogous massive overproduction of NS-XRBs in a different dense environment (globular clusters). While suggestive, this analogy is incomplete: NS-XRBs are dynamically manufactured in globulars by exchange interactions (e.g. binary-single scatterings), but this mechanism is disfavored in the GC’s high velocity dispersion environment, which only permits the survival of the hardest main sequence binaries.

We instead propose that the observed LMXBs are formed via tidal capture of low mass stars by BHs. We estimated the distribution of stars and compact remnants in the GC using time-dependent Fokker-Planck models that predict close encounter rates. Taken at face value, tidal capture can explain the observed (and extrapolated) inventory of BH-XRBs in the GC. Our primary results are summarized as follows:

- (i) We calculated the rate at which low mass stars are tidally captured by BHs and NS as a function of time, and used this to predict that there should be ~ 60 -200 accreting BH-XRBs in the central parsec today. The number and radial distribution of these binaries is consistent with the quiescent BH-XRB population identified by [Hailey et al. \(2018\)](#), given reasonable extrapolation below the *Chandra* detection threshold.

Table 4. Present-day rates of various “exotic” collisional stellar interactions in our GC models. From top to bottom: physical collisions between ordinary stars, close encounters between BHs and red giants that would remove a significant fraction of the latter’s envelope ($r_p \lesssim 15R_\odot$), disruptions of ordinary stars by the central SMBH and by smaller mass remnants, BH-BH binary formation by bound-free gravitational wave emission, ejection of stars from the GC in strong scatterings with BHs.

| Interaction | Fiducial | Fiducial $\times 10$ |
|---|-----------------------|-----------------------|
| Star-star collisions [yr^{-1}] | 7×10^{-6} | 7×10^{-6} |
| BH-Red giant collisions [yr^{-1} giant $^{-1}$ at 0.1 pc] | 5×10^{-11} | 1.5×10^{-10} |
| micro-TDEs (BH) [yr^{-1}] | 6×10^{-7} | 2×10^{-6} |
| micro-TDEs (NS) [yr^{-1}] | 9×10^{-8} | 3×10^{-7} |
| TDEs (SMBH) [yr^{-1}] | 10^{-4} | 2×10^{-4} |
| GW bound-free captures (BH-BH) [yr^{-1}] | 1.4×10^{-10} | 1.1×10^{-9} |
| Ejection of stars by strong scattering [yr^{-1}] | 3×10^{-4} | 10^{-3} |

(ii) Our models also produced a substantial number of NS-XRBs (far more than are currently observed). However, there are several candidate mechanisms for suppressing our predicted NS-XRB population. Alternatively, evolved NS binaries may also manifest as MSPs, whose population is poorly constrained in the GC.

(iii) The compact object source terms in our Fokker-Planck models were calibrated from the observed number of massive stars in the GC. Most of the stellar mass BHs in the GC may originate in star forming disks with a top heavy IMF, like the one currently observed at $\sim 10^{18}$ cm (Krabbe et al. 1995; Paumard et al. 2006; Bartko et al. 2010; Lu et al. 2013). In our models, *in situ* star formation in these disks has left between 10^4 and 4×10^4 BHs within the central parsec, at $z = 0$. Much smaller numbers of BHs would fail to explain the observed BH-XRB population, yielding the first quantitative constraints on the long-theorized “dark cusp” in the GC.

(iv) We also estimated the rates of other exotic dynamical interactions between stars and compact objects. For example, we found that the rate of disruption of stars by stellar mass BHs (“micro-tidal disruption”) in the Galactic Center is $\sim 10^{-6}$ per year—comparable to previous estimates of the total rate in the field and globular clusters (Perets et al. 2016), as well as the rate of ultra-long GRBs (Levan et al. 2014). The present-day TDE rate from Sgr A* is $\sim 1 - 3 \times 10^{-4} \text{ yr}^{-1}$, similar to other SMBHs of its mass.

The largest theoretical uncertainty in our model is the assumption that main sequence stars tidally captured by stellar mass BHs are able to circularize and settle into stable Roche-lobe overflow. Such an outcome is not energetically guaranteed, and it is likely that BHs above a certain mass will rapidly destroy tidally captured stars by thermalizing too much mode energy inside them, leading to super-Eddington accretion in a string of partial tidal disruptions. The precise BH mass threshold above which tidal capture becomes catastrophic is an open question that we hope to address in future work. A second concern is that tidal capture binaries have periods $\lesssim 10$ hours. In the field, such systems have low X-ray luminosities, and, if placed in the GC, would fall below the Chandra detection threshold. However, short period field XRBs likely have a different formation mechanism, and it is not clear if tidal capture XRBs would inherit their luminosity function.

While we have focused on tidal capture in an isotropized

population of stars and compact objects, it may be fruitful to examine high mass XRB formation within star-forming disks. The small number of high mass stars in the Galactic Center and their short lifetimes suggest that the number of high mass XRBs would be small. However, the capture rate of disk stars is enhanced by (i) their larger cross-section (which scales linearly with the star’s mass if the star is more massive than the BH) (ii) their larger escape speeds (iii) the enhanced stellar densities within the star-forming disk. We would expect ~ 0.3 HMXBs from BHs interacting with the disk of young stars in our Fiducial model. This number would increase by up to two orders of magnitude if the stellar mass BHs are aligned with the stellar disks as in Szölygény & Kocsis (2018). It is also possible that stellar mass objects migrating within a gaseous disk may smoothly capture into binaries due to gas dissipation alone, even in the absence of strong tidal coupling. While there are no HMXBs present in the GC today (Hailey et al. 2018), past or extragalactic populations of nuclear HMXBs are potentially interesting as progenitors of LIGO-band GW sources.

Our tidal capture model was motivated by surprising discoveries in the MW Center, but it carries major implications for extragalactic NSCs as well. If the GC’s inventory of XRBs is representative, it may complicate X-ray searches for low-luminosity intermediate mass black hole AGN in dwarf galaxies. The unresolved, integrated X-ray luminosity from a large XRB population represents a durable if dim contaminant; a single BH-XRB in outburst would represent a more dangerous contaminant for single-epoch searches. The existence of dark cusps in galactic nuclei also carries major implications for the highly uncertain rates of extreme mass ratio inspirals, one of the primary scientific targets for future space-based GW laser interferometers (e.g. *eLISA*). Future dynamical modeling of XRB formation in the GC may yield more sophisticated constraints on the radial profile of our dark cusp, a local laboratory with which we may calibrate our expectations for stellar dynamics in distant galactic nuclei.

ACKNOWLEDGMENTS

We thank the referee for helpful and insightful comments. We are happy to acknowledge useful discussions with Fabio Antonini, Josh Grindlay, Nathan Leigh, Nevin Weinberg, Doug Lin, Eugene Vasiliev, Jessica Lu and Jules Halpern.

We are especially grateful to Charles Hailey for discussions of his recent observational findings. NCS received financial support from NASA through Einstein Postdoctoral Fellowship Award Number PF5-160145, and thanks the Aspen Center for Physics for its hospitality during the completion of this work. BDM and AG acknowledge support from NSF Astronomy and Astrophysics grants AST-1410950, AST-1615084; NASA Astrophysics Theory Program grants NNX16AB30G, NNX17AK43G; and Hubble Space Telescope Grant HST-GO-14785.004-A.

APPENDIX A: TIDAL COUPLING CONSTANTS

The energy deposited into a star of mass m_* after a close encounter with a compact object of mass m_c is given by

$$\Delta E = \frac{Gm_*^2}{r_*} \left(\frac{m_c}{m_*}\right)^2 \sum_{l=2}^{\infty} T_l(\eta) \left(\frac{r_*}{r_p}\right)^{(2l+2)}$$

$$\eta \equiv \left(\frac{m_*}{m_* + m_c}\right)^{1/2} \left(\frac{r_*}{r_p}\right)^{-3/2}, \quad (\text{A1})$$

where r_p is the pericenter distance of the encounter, r_* is the radius of the star, and T_l is the tidal coupling constant of multipole order l , which depends on the stellar structure and orbit.

For fixed stellar structure, the tidal coupling constant is a function of the ratio η of the star's dynamical time to the time spent near pericenter. For the dominant $l = 2$ modes the energy deposited in the star is

$$\Delta E = T_2(\eta) \left(\frac{r_p}{r_t}\right)^{-6} \frac{Gm_*^2}{r_*}, \quad (\text{A2})$$

where $r_t = r_*(m_c/m_*)^{1/3}$ is the tidal radius.

Fig. A1 compares the $l = 2$ tidal coupling constants for both polytropic and MESA stellar models (Paxton et al. 2011, 2013).¹³ Calculating the tidal coupling constant requires a summation over discrete stellar eigenmodes, which we calculate with GYRE (Townsend & Teitler 2013).¹⁴ Following Lee & Ostriker (1986), we include the f-mode, the five lowest order p-modes, and the eighteen lowest order g-modes (if they exist) in the summation.

For stars of mass $\lesssim 0.3 M_\odot$, g-modes are not excited at all and most of the energy is deposited into the f-mode. Larger stellar masses and larger values of r_p result in greater energy transfer into g-modes, while p-modes are always subdominant. Fig. A2 shows the fraction of energy placed into different modes as a function of pericenter for $m_* = 0.3 M_\odot$ and $m_* = 1 M_\odot$ stars. An $n = 3/2$ polytropic model accurately reproduces the mode spectrum of the low mass star. However, the mode spectrum of the solar type star is poorly approximated by a polytropic model: the $n = 3$ polytropic model underestimates the energy in g-modes, and overestimates that in the f-mode, for small pericenter distances.

The tidal coupling constant of low mass stars ($m_* \lesssim 0.5 M_\odot$), is close to that of an $n = 3/2$ polytrope. The tidal coupling constant approaches that of an $n = 3$ polytrope as the stellar mass approaches $1 M_\odot$.

APPENDIX B: CORRECTIONS FOR NON-LINEAR EFFECTS

Linear theory underestimates the energy deposited in the star by a factor of a few for the close pericenters of interest. Non-linear corrections have been calculated by Ivanov & Novikov (2001) for polytropic stellar models. We adopt their prescriptions for the tidal coupling constant for close pericenters.

¹³ <http://mesa.sourceforge.net>, version 9575

¹⁴ <https://bitbucket.org/rhdtownsend/gyre/wiki/Home>, version 5. We assume adiabatic oscillations.

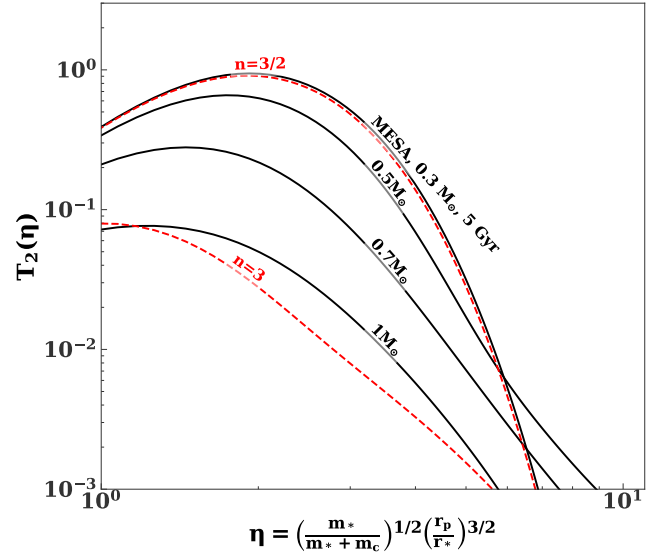


Figure A1. Comparison of tidal coupling constant as a function of η (eq. A1) for different stellar models as labeled. The dashed, red lines show the tidal coupling constants for polytropic stellar models. We have assumed a parabolic orbit.

Fig. B1 compares tidal coupling constants for polytropic models from linear theory and from Ivanov & Novikov (2001) (see also their Figures 13 and 15). The following expressions reproduce tidal coupling constants from Ivanov & Novikov (2001) for small pericenters, while approaching the results of linear theory at large pericenters.

$n=3/2$ polytrope:

$$T(\eta) = C 2^{(b-g)/s} \left(\frac{\eta}{\eta_o}\right)^{-g} \left(1 + \left(\frac{\eta}{\eta_o}\right)^s\right)^{(g-b)/s}$$

$$\times \left(\frac{1}{2} - \frac{1}{2} \tanh \left[k \left(\frac{r}{r_1} - 1\right) \right]\right)$$

$$C = 2.58, \eta_o = 1.73, g = -4.36, b = 2.82, s = 9.91,$$

$$r_1 = 4.5, k = 4 \quad (\text{B1})$$

$n=3$ polytrope:

$$T(\eta) = C 2^{(b-g)/s} \left(\frac{\eta}{\eta_o}\right)^{-g} \left(1 + \left(\frac{\eta}{\eta_o}\right)^s\right)^{(g-b)/s}$$

$$\times \left(1 + \left(\frac{\eta}{\eta_1}\right)^{s_2}\right)^{(b-b_2)/s_2}$$

$$C = 0.17, \eta_o = 1.07, \eta_1 = 1.92, g = -3.83,$$

$$b = 5.5, b_2 = 3.49, s = 3.59, s_2 = 6.68, \quad (\text{B2})$$

where we have adopted eq. (B1) for low mass stars with $m_* \leq 0.7 M_\odot$, and eq. (B2) for higher stellar masses.

APPENDIX C: BINARY EXCHANGE INTERACTIONS

C1 Binary fraction

When *soft* binaries interact with field stars in the GC they gain energy, become more loosely bound, and eventually dissociate (Heggie 1975; Binney & Tremaine 1987). A binary

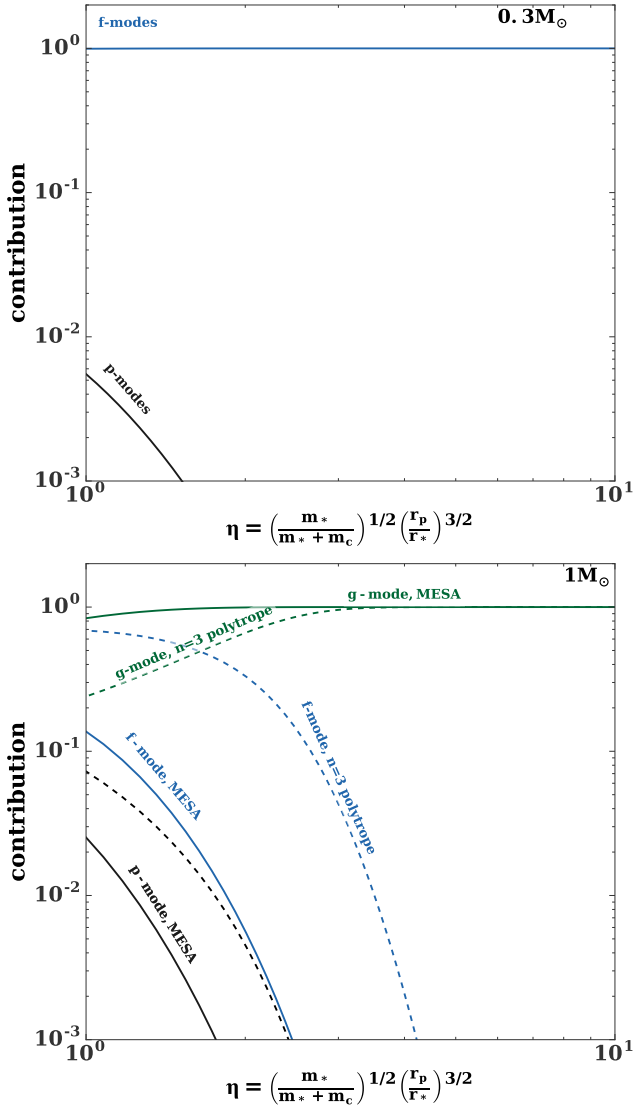


Figure A2. *Top panel:* Fraction of oscillation energy deposited into p-, f-, and g-modes for a star of mass $0.3M_{\odot}$. For this calculation we use a MESA model evolved for 5 Gyr, but the results are indistinguishable from that of an $n = 3/2$ polytrope. The g-modes do not contribute. *Bottom panel:* Same as the top panel, but for a star of mass $1 M_{\odot}$. The mode decomposition is not accurately reproduced by a polytropic model, as can be seen by comparing the solid and dashed lines.

is soft if its binding energy is less than the kinetic energy of a typical field star, i.e. if,

$$\frac{Gm_1m_2}{a\langle m \rangle} < \sigma^2, \quad (\text{C1})$$

where m_1 and m_2 are the masses of the binary components, a is the semi-major axis, $\langle m \rangle$ is the mean stellar mass, and σ is the 1D velocity dispersion. Binaries that do not satisfy eq. (C1) are *hard*. Interactions with field stars shrink the separation of a hard binary over time, making it a smaller target. Thus, it is much easier (and faster) to dissolve a soft binary than to push a hard binary to coalescence.

The black lines in Fig. C1 shows the hard-soft boundary

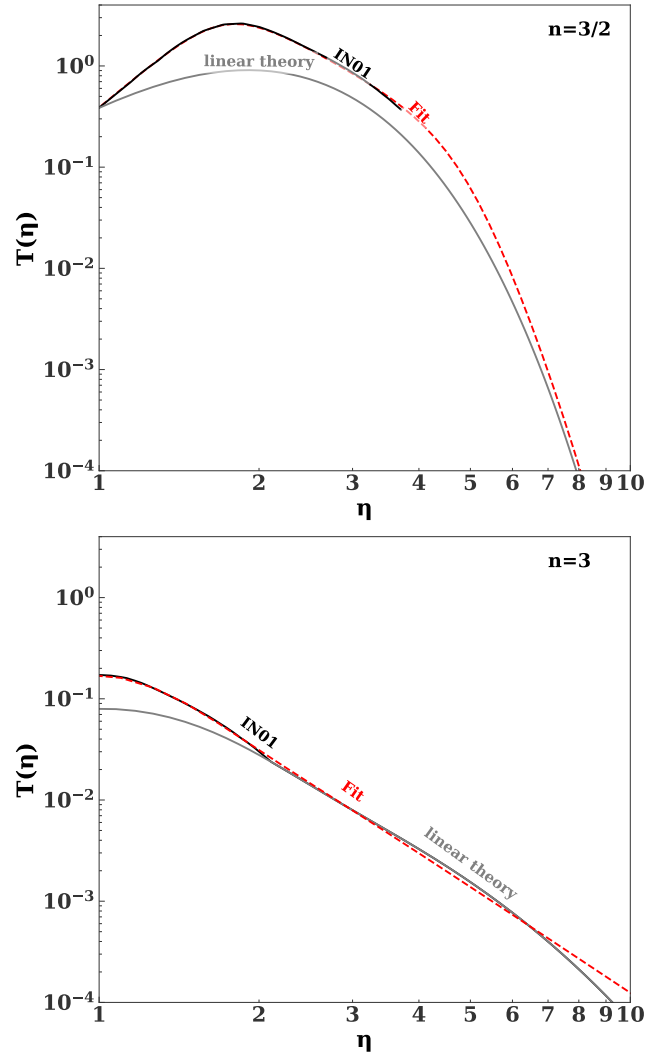


Figure B1. Fitted tidal coupling constants $T(\eta)$ from the non-linear results of Ivanov & Novikov (2001). Results are shown for $n = 3/2$ (top panel) and $n = 3$ (bottom panel) polytropes.

in our Fiducial model of the Galactic Center for two different binary masses. For a binary distribution that is flat in $\log(a)$, from the semi-major axis of Roche-Lobe contact $a_{\text{roche}} \approx r_t \sim R_{\star}$ to $a = 900$ AU, we find that $\sim 73\%$ (87%) of binaries with two solar mass (0.3 solar mass stars) are soft at 1 pc. By contrast, in a globular cluster with $\sigma \sim 10$ km s $^{-1}$, only 40–50% of the primordial binaries are soft (Ivanova et al. 2005).

Soft binaries can be ionized in two different ways:

a Direct collisions with field stars, as occurs on a timescale

$$\tau_{\text{collide}} = \frac{1}{\pi n_{\star} \sigma a^2 \left(1 + \frac{2G(m_1+m_2)}{\sigma^2 a} \right)}. \quad (\text{C2})$$

In our fiducial models, the collision rate of binaries with stars exceeds the collision rate of binaries with compact objects.

b “Evaporation” due to perturbations from distant field

stars. For an equal mass binary this occurs on a timescale (Alexander & Pfuhl 2014; their eq. 3)

$$\tau_{\text{evap}} \approx 0.07 \frac{(m_1 + m_2)\sigma}{Gn\langle m^2 \rangle \ln \Lambda}, \quad (\text{C3})$$

where m_{bin} is the total mass of the binary, n is the number density of perturbers, $\langle m^2 \rangle$ is the second moment of the mass function, σ is the 1D velocity dispersion, and $\ln \Lambda \approx 15$ is the Coulomb logarithm.

The red lines in Fig. C1 show the semi-major axes for which the collision and evaporation times are equal to 10^{10} years. Any primordial binaries with semi-major axes $\gtrsim 0.1$ AU within the central parsec would be evaporated on a timescale of $\lesssim 10^{10}$ yr.

On the other hand, binaries with particularly *small* semi-major axes can be destroyed by magnetic braking. Following Ivanova & Kalogera (2006) (their eq. 4), we find that two stars of mass m_* with semi-major axes obeying

$$a < 3 \left(\frac{m_*}{M_\odot} \right)^{0.16} \left(\frac{t}{10 \text{ Gyr}} \right)^{0.41} a_{\text{roche}}, \quad (\text{C4})$$

are brought into Roche-Lobe contact after time t . Solar mass stars in a two day orbit would thus come into Roche-Lobe contact within $\lesssim 5$ Gyr (see also Andronov et al. 2006).

The binary fraction is

$$f_b \equiv \frac{N_b}{N_s + N_b} = \frac{(1 - f_d)f_{b,0}}{1 + f_d f_{b,0}} \quad (\text{C5})$$

where N_b and N_s are the numbers of single stars and binaries respectively, $f_{b,0}$ is the initial binary fraction and f_d is the fraction that are destroyed due to the effects of evaporation and/or magnetic braking. Figure C2 shows the expected binary fraction at 1 pc after 5 and 10 Gyr, as a function of stellar mass (assuming equal mass binaries). Weighting each mass bin by a Kroupa PDMF, we find that the binary fraction is $\sim 4\%$ (3%) after 5 (10) Gyr. Our estimate for the binary fraction of solar mass stars accounting evaporation alone ($\sim 10\%$) is comparable to previous estimates (Hopman 2009).

Kozai-Lidov (KL) oscillations induced by the central SMBH can turn some soft binaries into hard binaries, effectively increasing the binary fraction. In particular, KL oscillations can excite binaries to very large eccentricities. Tides can then dissipate energy, creating a tight stellar binary (Antonini & Perets 2012; Stephan et al. 2016). In practice, for the Galactocentric radii of interest (~ 1 pc), the time-scale to excite the binary to very large eccentricities (the *octupole* Kozai time scale) is generally longer than the evaporation time-scale. Additionally, for a $1M_\odot$ binary, GR precession will damp KL oscillations for binary separations

$$a_1 < 2 \text{ au} \left(\frac{a_2}{1 \text{ pc}} \right)^{3/4} \frac{(1 - e_2^2)^{3/8}}{(1 - e_1^2)^{1/4}}, \quad (\text{C6})$$

where e_1 is the eccentricity of the inner binary orbit, while a_2 and e_2 are the semi-major axis and eccentricity of the binary's orbit around the SMBH (see equation 59 in Naoz 2016).

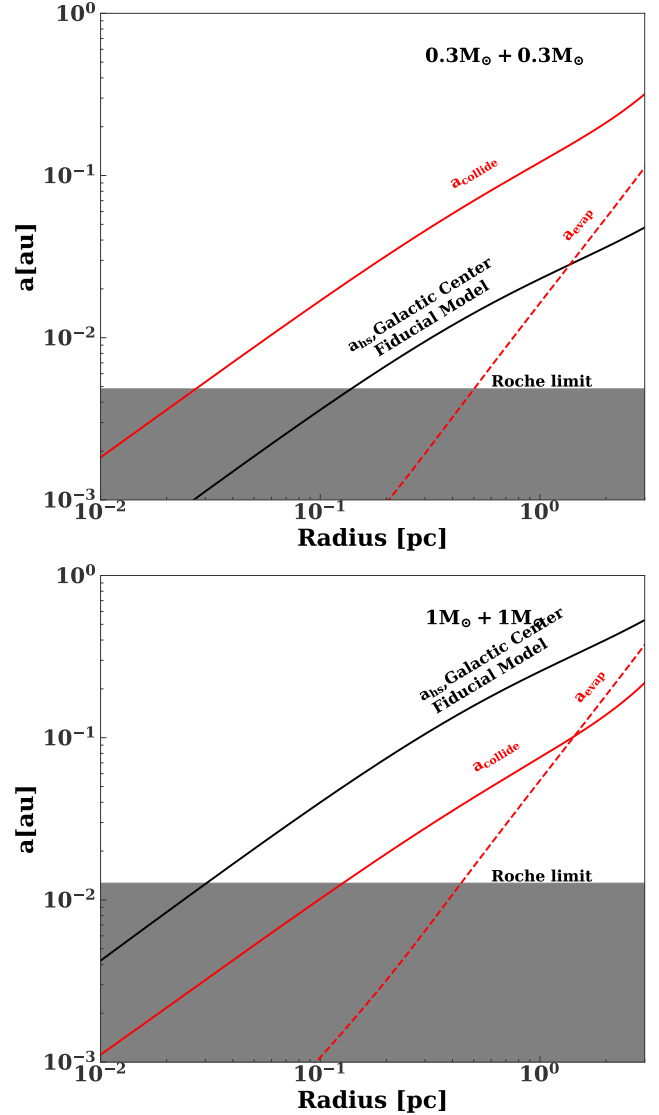


Figure C1. Hard-soft boundary for $1+1 M_\odot$ (top panel) and $0.3+0.3 M_\odot$ (bottom panel) in our fiducial model for the GC. The red lines show the semi-major axis for which the time-scale for direct collisions (eq. C2) and evaporation (eq. C3) is 10^{10} years. Binaries in the gray region are either contact binaries or unphysical as the semi-major axis of the binary would be smaller than the Roche limit.

C2 Binary exchange rates

Finally, the rate of compact objects exchanging into existing stellar binaries is

$$\dot{n}_{2+1} = \int_0^\infty n_c f_b n_* \Sigma v_\infty f(v_\infty) dv_\infty, \quad (\text{C7})$$

where n_c and n_* are the densities of compact objects (BHs or NSs) and stars, respectively, and Σ is the total cross-section for the compact object to be captured into a binary with an ordinary star. This may either occur via a *prompt exchange* or a *resonant capture*. In the former case the exchange occurs quickly, while in the latter case a metastable triple system is formed first. The cross-sections for these processes have been calibrated from binary-single scattering experiments as

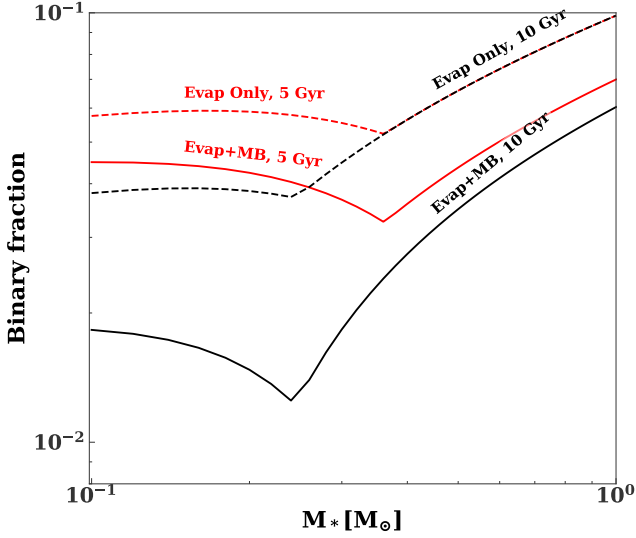


Figure C2. Binary fraction at 1 pc after 5 Gyr (red lines) and 10 (black lines) Gyr, calculated for an assumed initial binary fraction of 50%. For the dashed lines we only account for evaporation of soft binaries, while for the solid lines we account for the destruction of hard binaries via magnetic braking. The x-axis indicates the mass of each of the stars in the binary.

(Valtonen & Karttunen 2006)

$$\Sigma_{\text{ex}} \approx 0.51 \frac{2m_c}{m_*} \frac{\pi a^2}{v^2} (1 - P_c) \quad (\text{C8})$$

$$\Sigma_{\text{cap}} \approx 1.18(n-1)(1-v^2)^{n-2} \frac{2m_c}{m_*} \frac{\pi a^2}{v^2} (1 - P_s) \quad (\text{C9})$$

$$P_c \approx 0.25(n-1)(1-v^2)^{n-2} \quad (\text{C10})$$

$$P_s = \frac{m_c^{-q}}{2m_*^{-q} + m_c^{-q}} \quad (\text{C11})$$

$$v^2 = \frac{2m_c}{M} \frac{v_\infty^2 a_o}{Gm_*}, \quad (\text{C12})$$

where m_c , m_* , and M are the masses of the compact object, the stars in the binary (assumed to be equal in mass), and the three-body system, respectively. The cross-sections go to 0 for $v \gtrsim 1$. The power law index n (q) depends on the angular momentum of the system, and is expected to vary between 4.5 and 3 (1 and 3) as v goes from 0 to 1. We choose $n = q = 3$, but the results are not very sensitive to this choice.

Using densities profiles of our Fiducial model, the rate of 2+1 encounters per unit volume at radii $\lesssim 1$ pc is approximately given by

$$\begin{aligned} \dot{n}_{\text{bh},2+1} &= 5 \times 10^{-11} \left(\frac{r}{1\text{pc}} \right)^{-2.5} \left(\frac{f_b}{0.01} \right) \left(\frac{m_*}{\bar{m}_*} \right) \text{pc}^{-3} \text{yr}^{-1} \\ \dot{n}_{\text{ns},2+1} &= 3 \times 10^{-11} \left(\frac{r}{1\text{pc}} \right)^{-1.9} \left(\frac{f_b}{0.01} \right) \left(\frac{m_*}{\bar{m}_*} \right) \text{pc}^{-3} \text{yr}^{-1} \end{aligned} \quad (\text{C13})$$

where $\bar{m}_* = 0.3M_\odot$. Integrating over volume and a Kroupa PDMF ($m_* = 0.2 - 1M_\odot$), we find that the total rate of 2+1

encounters inside of 1 pc is

$$\begin{aligned} \dot{N}_{\text{bh},2+1} &= 8 \times 10^{-10} \left(\frac{f_b}{0.01} \right) \text{yr}^{-1} \\ \dot{N}_{\text{ns},2+1} &= 4 \times 10^{-10} \left(\frac{f_b}{0.01} \right) \text{yr}^{-1}, \end{aligned} \quad (\text{C14})$$

where we have truncated the volume integral where a_{hs} equals the stellar radius. Comparing to the tidal capture rates (Fig. 11), we see the rate of 2+1 encounters is subdominant for binary fractions of $\lesssim 50\%$ for BHs and 15% for NSs, as expected in the GC from the above considerations. We stress that these calculations are generous to the 2+1 formation channel, as we have assumed that every exchange interaction involving a main sequence binary and a compact object will lead to XRB formation, while in reality this is only true for a subset of these interactions. For example, three-body interactions can result in a physical stellar collision (Fregeau et al. 2004). Thus, for the low binary fractions expected in the GC, binary-single exchange interactions should be highly subdominant to tidal capture in the formation of XRBs.

REFERENCES

- Abbate F., Mastrobuono-Battisti A., Colpi M., Possenti A., Sip- pel A. C., Dotti M., 2018, *MNRAS*, **473**, 927
- Aharon D., Perets H. B., 2015, *ApJ*, **799**, 185
- Aharon D., Mastrobuono Battisti A., Perets H. B., 2016, *ApJ*, **823**, 137
- Alexander T., Hopman C., 2009, *ApJ*, **697**, 1861
- Alexander T., Kumar P., 2001, *ApJ*, **549**, 948
- Alexander T., Morris M., 2003, *ApJ*, **590**, L25
- Alexander T., Pfuhl O., 2014, *ApJ*, **780**, 148
- Amaro-Seoane P., Chen X., 2014, *ApJ*, **781**, L18
- Andronov N., Pinsonneault M. H., Terndrup D. M., 2006, *ApJ*, **646**, 1160
- Antonini F., Perets H. B., 2012, *ApJ*, **757**, 27
- Antonini F., Rasio F. A., 2016, *ApJ*, **831**, 187
- Antonini F., Capuzzo-Dolcetta R., Mastrobuono-Battisti A., Merritt D., 2012, *ApJ*, **750**, 111
- Arca-Sedda M., Capuzzo-Dolcetta R., 2014, *MNRAS*, **444**, 3738
- Arca-Sedda M., Kocsis B., Brandt T., 2017, preprint, ([arXiv:1709.03119](https://arxiv.org/abs/1709.03119))
- Arcavi I., et al., 2014, *ApJ*, **793**, 38
- Armas Padilla M., Wijnands R., Degenaar N., Muñoz-Darias T., Casares J., Fender R. P., 2014, *MNRAS*, **444**, 902
- Askar A., Arca Sedda M., Giersz M., 2018, preprint, ([arXiv:1802.05284](https://arxiv.org/abs/1802.05284))
- Auchettl K., Guillochon J., Ramirez-Ruiz E., 2017, *ApJ*, **838**, 149
- Bahcall J. N., Wolf R. A., 1976, *ApJ*, **209**, 214
- Bahcall J. N., Wolf R. A., 1977, *ApJ*, **216**, 883
- Bahramian A., et al., 2014, *ApJ*, **780**, 127
- Bahramian A., et al., 2017, *MNRAS*, **467**, 2199
- Banerjee S., Baumgardt H., Kroupa P., 2010, *MNRAS*, **402**, 371
- Bar-Or B., Alexander T., 2016, *ApJ*, **820**, 129
- Bartko H., et al., 2010, *ApJ*, **708**, 834
- Bartos I., Kocsis B., Haiman Z., Márka S., 2017, *ApJ*, **835**, 165
- Baumgardt H., Amaro-Seoane P., Schödel R., 2018, *A&A*, **609**, A28
- Benacquista M. J., Downing J. M. B., 2013, *Living Reviews in Relativity*, **16**, 4
- Binney J., Tremaine S., 1987, *Galactic dynamics*
- Blagorodnova N., et al., 2017, *ApJ*, **844**, 46

- Bower G. C., Roberts D. A., Yusef-Zadeh F., Backer D. C., Cotton W. D., Goss W. M., Lang C. C., Lithwick Y., 2005, *ApJ*, **633**, 218
- Brandt T. D., Kocsis B., 2015, *ApJ*, **812**, 15
- Breen P. G., Heggie D. C., 2012, *MNRAS*, **425**, 2493
- Breen P. G., Heggie D. C., 2013, *MNRAS*, **432**, 2779
- Buchholz R. M., Schödel R., Eckart A., 2009, *A&A*, **499**, 483
- Chornock R., et al., 2014, *ApJ*, **780**, 44
- Cohn H., 1985, in Goodman J., Hut P., eds, IAU Symposium Vol. 113, Dynamics of Star Clusters. pp 161–177
- Corral-Santana J. M., Casares J., Muñoz-Darias T., Bauer F. E., Martínez-Pais I. G., Russell D. M., 2016, *A&A*, **587**, A61
- Dale J. E., Davies M. B., Church R. P., Freitag M., 2009, *MNRAS*, **393**, 1016
- Degenaar N., Wijnands R., 2010, *A&A*, **524**, A69
- Degenaar N., Wijnands R., Miller J. M., Reynolds M. T., Kennea J., Gehrels N., 2015, *Journal of High Energy Astrophysics*, **7**, 137
- Do T., Ghez A. M., Morris M. R., Lu J. R., Matthews K., Yelda S., Larkin J., 2009, *ApJ*, **703**, 1323
- Donley J. L., Brandt W. N., Eracleous M., Boller T., 2002, *AJ*, **124**, 1308
- Dubus G., Lasota J.-P., Hameury J.-M., Charles P., 1999, *MNRAS*, **303**, 139
- Fabian A. C., Pringle J. E., Rees M. J., 1975, *MNRAS*, **172**, 15p
- Fragione G., Sari R., 2018, *ApJ*, **852**, 51
- Frank J., King A., Raine D. J., 2002, *Accretion Power in Astrophysics: Third Edition*
- Fregeau J. M., Cheung P., Portegies Zwart S. F., Rasio F. A., 2004, *MNRAS*, **352**, 1
- Freitag M., Amaro-Seoane P., Kalogera V., 2006, *ApJ*, **649**, 91
- Fuller J., Lai D., 2011, *MNRAS*, **412**, 1331
- Fuller J., Lai D., 2012, *MNRAS*, **421**, 426
- Genzel R., Thatte N., Krabbe A., Kroker H., Tacconi-Garman L. E., 1996, *ApJ*, **472**, 153
- Genzel R., et al., 2003, *ApJ*, **594**, 812
- Georgiev I. Y., Böker T., 2014, *MNRAS*, **441**, 3570
- Gezari S., et al., 2006, *ApJ*, **653**, L25
- Gezari S., et al., 2008, *ApJ*, **676**, 944
- Gezari S., et al., 2012, *Nature*, **485**, 217
- Gnedin O. Y., Ostriker J. P., Tremaine S., 2014, *ApJ*, **785**, 71
- Greiner J., et al., 2015, *Nature*, **523**, 189
- Guetta D., Piran T., Waxman E., 2005, *ApJ*, **619**, 412
- Guillochon J., Ramirez-Ruiz E., 2013, *ApJ*, **767**, 25
- Habibi M., et al., 2017, *ApJ*, **847**, 120
- Hailey C. J., Mori K., 2017, in AAS/High Energy Astrophysics Division. p. 109.12
- Hailey C. J., Mori K., Bauer F. E., Berkowitz M. E., Hong J., Hord B. J., 2018, *Nature*, 556, 70
- Hayasaki K., Zhong S., Li S., Berczik P., Spurzem R., 2018, *ApJ*, **855**, 129
- Heggie D. C., 1975, *MNRAS*, **173**, 729
- Heinke C. O., Grindlay J. E., Edmonds P. D., 2005a, *ApJ*, **622**, 556
- Heinke C. O., Grindlay J. E., Edmonds P. D., Cohn H. N., Lugger P. M., Camilo F., Bogdanov S., Freire P. C., 2005b, *ApJ*, **625**, 796
- Heinke C. O., Wijnands R., Cohn H. N., Lugger P. M., Grindlay J. E., Pooley D., Lewin W. H. G., 2006, *ApJ*, **651**, 1098
- Henon M., 1969, *A&A*, **2**, 151
- Hills J. G., 1975, *Nature*, **254**, 295
- Hobbs G., Lorimer D. R., Lyne A. G., Kramer M., 2005, *MNRAS*, **360**, 974
- Holoien T. W.-S., et al., 2014, *MNRAS*, **445**, 3263
- Holoien T. W.-S., et al., 2016a, *MNRAS*, **455**, 2918
- Holoien T. W.-S., et al., 2016b, *MNRAS*, **463**, 3813
- Hopman C., 2009, *ApJ*, **700**, 1933
- Hopman C., Alexander T., 2006a, *ApJ*, **645**, 1152
- Hopman C., Alexander T., 2006b, *ApJ*, **645**, L133
- Hurley J. R., Pols O. R., Tout C. A., 2000, *MNRAS*, **315**, 543
- Ivanov P. B., Novikov I. D., 2001, *ApJ*, **549**, 467
- Ivanova N., Kalogera V., 2006, *ApJ*, **636**, 985
- Ivanova N., Belczynski K., Fregeau J. M., Rasio F. A., 2005, *MNRAS*, **358**, 572
- Ivanova N., Heinke C. O., Rasio F. A., Belczynski K., Fregeau J. M., 2008, *MNRAS*, **386**, 553
- Katz J. I., 1975, *Nature*, **253**, 698
- Kieffer T. F., Bogdanović T., 2016, *ApJ*, **823**, 155
- Kochanek C. S., 1992, *ApJ*, **385**, 604
- Kochanek C. S., 2016, *MNRAS*, **461**, 371
- Krabbe A., et al., 1995, *ApJ*, **447**, L95
- Kremer K., Chatterjee S., Rodriguez C. L., Rasio F. A., 2018a, *ApJ*, **852**, 29
- Kremer K., Ye C. S., Chatterjee S., Rodriguez C. L., Rasio F. A., 2018b, *ApJ*, **855**, L15
- Kulkarni S. R., Hut P., McMillan S., 1993, *Nature*, **364**, 421
- Kumar P., Goodman J., 1996, *ApJ*, **466**, 946
- Lee H. M., Ostriker J. P., 1986, *ApJ*, **310**, 176
- Leigh N. W. C., Antonini F., Stone N. C., Shara M. M., Merritt D., 2016, *MNRAS*, **463**, 1605
- Leigh N. W. C., et al., 2018, *MNRAS*, **474**, 5672
- Levan A. J., et al., 2014, *ApJ*, **781**, 13
- Levin Y., Beloborodov A. M., 2003, *ApJ*, **590**, L33
- Lin D. N. C., Tremaine S., 1980, *ApJ*, **242**, 789
- Linial I., Sari R., 2017, *MNRAS*, **469**, 2441
- Loutrel N., Yunes N., Pretorius F., 2014, *Phys. Rev. D*, **90**, 104010
- Lu J. R., Do T., Ghez A. M., Morris M. R., Yelda S., Matthews K., 2013, *ApJ*, **764**, 155
- Maccarone T. J., Kundu A., Zepf S. E., Rhode K. L., 2007, *Nature*, **445**, 183
- Mackey A. D., Wilkinson M. I., Davies M. B., Gilmore G. F., 2008, *MNRAS*, **386**, 65
- Mainetti D., Lupi A., Campana S., Colpi M., Coughlin E. R., Guillochon J., Ramirez-Ruiz E., 2017, *A&A*, **600**
- Manukian H., Guillochon J., Ramirez-Ruiz E., O’Leary R. M., 2013, *ApJ*, **771**, L28
- Mardling R. A., 1995, *ApJ*, **450**, 722
- McCourt M., Madigan A.-M., 2016, *MNRAS*, **455**, 2187
- Merritt D., 2010, *ApJ*, **718**, 739
- Merritt D., 2013, Dynamics and Evolution of Galactic Nuclei
- Merritt D., 2015, *ApJ*, **804**, 52
- Metzger B. D., Stone N. C., 2016, *MNRAS*, **461**, 948
- Miller-Jones J. C. A., et al., 2015, *MNRAS*, **453**, 3918
- Miralda-Escudé J., Gould A., 2000, *ApJ*, **545**, 847
- Mori K., et al., 2013, *ApJ*, **770**, L23
- Morris M., 1993, *ApJ*, **408**, 496
- Morscher M., Umbreit S., Farr W. M., Rasio F. A., 2013, *ApJ*, **763**, L15
- Morscher M., Pattabiraman B., Rodriguez C., Rasio F. A., Umbreit S., 2015, *ApJ*, **800**, 9
- Muno M. P., Pfahl E., Baganoff F. K., Brandt W. N., Ghez A., Lu J., Morris M. R., 2005, *ApJ*, **622**, L113
- Naoz S., 2016, *ARA&A*, **54**, 441
- O’Leary R. M., Kocsis B., Loeb A., 2009, *MNRAS*, **395**, 2127
- Paczynski B., Trimble V., 1979, in Burton W. B., ed., IAU Symposium Vol. 84, The Large-Scale Characteristics of the Galaxy. pp 401–403
- Paumard T., et al., 2006, *ApJ*, **643**, 1011
- Paxton B., Bildsten L., Dotter A., Herwig F., Lesaffre P., Timmes F., 2011, *ApJS*, **192**, 3
- Paxton B., et al., 2013, *ApJS*, **208**, 4
- Peebles P. J. E., 1972, *ApJ*, **178**, 371
- Perets H. B., Li Z., Lombardi Jr. J. C., Milcarek Jr. S. R., 2016, *ApJ*, **823**, 113
- Perez K., et al., 2015, *Nature*, **520**, 646
- Peters P. C., 1964, *Physical Review*, **136**, 1224

- Pfahl E., Loeb A., 2004, *ApJ*, **615**, 253
- Pfuhl O., et al., 2011, *ApJ*, **741**, 108
- Press W. H., Teukolsky S. A., 1977, *ApJ*, **213**, 183
- Quinlan G. D., Shapiro S. L., 1987, *ApJ*, **321**, 199
- Rauch K. P., Tremaine S., 1996, *New A*, **1**, 149
- Rees M. J., 1988, *Nature*, **333**, 523
- Sazonov S., Sunyaev R., Revnivtsev M., 2012, *MNRAS*, **420**, 388
- Schödel R., Gallego-Cano E., Dong H., Nogueras-Lara F., Gallego-Calvente A. T., Amaro-Seoane P., Baumgardt H., 2018, *A&A*, **609**, A27
- Spitzer L., 1987, Dynamical evolution of globular clusters
- Stephan A. P., Naoz S., Ghez A. M., Witzel G., Sitarski B. N., Do T., Kocsis B., 2016, *MNRAS*, **460**, 3494
- Stone N. C., Metzger B. D., 2016, *MNRAS*, **455**, 859
- Stone N. C., Metzger B. D., Haiman Z., 2017a, *MNRAS*, **464**, 946
- Stone N. C., Küpper A. H. W., Ostriker J. P., 2017b, *MNRAS*, **467**, 4180
- Strader J., Chomiuk L., Maccarone T. J., Miller-Jones J. C. A., Seth A. C., 2012a, *Nature*, **490**, 71
- Strader J., Chomiuk L., Maccarone T. J., Miller-Jones J. C. A., Seth A. C., Heinke C. O., Sivakoff G. R., 2012b, *ApJ*, **750**, L27
- Sukhbold T., Ertl T., Woosley S. E., Brown J. M., Janka H.-T., 2016, *ApJ*, **821**, 38
- Szölgvény Á., Kocsis B., 2018, preprint, ([arXiv:1803.07090](https://arxiv.org/abs/1803.07090))
- Tetarenko B. E., et al., 2016, *ApJ*, **825**, 10
- Townsend R. H. D., Teitler S. A., 2013, *MNRAS*, **435**, 3406
- Tremaine S. D., Ostriker J. P., Spitzer Jr. L., 1975, *ApJ*, **196**, 407
- Tsang D., 2013, *ApJ*, **777**, 103
- Valtonen M., Karttunen H., 2006, *The Three-Body Problem*
- Vasiliev E., 2017, *ApJ*, **848**, 10
- Vinkó J., et al., 2015, *ApJ*, **798**, 12
- Wang J., Merritt D., 2004, *ApJ*, **600**, 149
- Wu Y., 2018, *AJ*, **155**, 118
- Yungelson L. R., Lasota J.-P., Nelemans G., Dubus G., van den Heuvel E. P. J., Dewi J., Portegies Zwart S., 2006, *A&A*, **454**, 559
- van Velzen S., 2018, *ApJ*, **852**, 72
- van Velzen S., Farrar G. R., 2014, *ApJ*, **792**, 53
- van Velzen S., et al., 2011, *ApJ*, **741**, 73